Design and Fabrication of a Magnetic Manipulator with

Five Degrees of Freedom

by

Pooriya Kazemzadeh Heris

A thesis

presented to the University of Waterloo

in fulfillment of the

thesis requirement for the degree of

Master of Applied Science

In

Mechanical and Mechatronics Engineering

Waterloo, Ontario, Canada, 2022

Author's Declaration

I hereby declare that I am the sole author of this thesis. This is a true copy of the thesis, including any required final revisions, as accepted by my examiners.

I understand that my thesis may be made electronically available to the public.

Abstract

Magnetic manipulation has the potential to recast the medical field both from an operational and drug delivery point of view as it can provide wireless controlled navigation over surgical devices and drug containers inside a human body. The accuracy and precision of controlled navigation will provide access to delicate organs and decrease the rehabilitation time. The advantages of achieving such a task have absorbed engineers' and researchers' attention and effort in the electromagnetic, imaging, mechanical, and robotic fields to implement the principles and make a functional magnetic manipulator.

The main idea behind magnetic manipulators is to regulate electrical currents fed to the coils to precisely position and orient an agent- also known as a robot or a magnetic tool- inside a working space. The presented system in this research is formed with nine coils, also known as electromagnets, placed normal to the spherical volume. The radius of this space is directly correlated with the dimensions and the number of coils, which can be utilized to parameterize the spatial constraints.

Extending the number of coils forming a spherical volume, also known as spherical workspace, has led to developing a unique geometrical constraint to optimize the coil placement. The determination of the constraints resulted in a specific outer diameter for each coil. In order to design a coil that produces the maximum axial force with the least power combustion with a given outer radius, Fabry Factor equation and Finite Element Method (FEM) were adopted. Fabry Factor relates the dimensions of the coils to each other such that the power consumption is minimized. Therefore, various iron-core coils were simulated using this method, and then the axial force of each coil at the furthest operational point in the working space was measured using FEM. The optimization result led to a cylindrical iron-core coil with an inner diameter of 20.5 mm, an outer diameter of 66 mm, and a length of 124 mm.

The FEM results in 3D for a complex system is mostly associated with errors between actual and simulated values of the magnetic field, around 17 percent less than the actual values in this project. In

order to eliminate this error, the magnetic field of the manufactured coil had been predicted using Artificial Intelligence (AI) techniques for experimental purposes. Regression models of Artificial Neural Network (ANN), a hybrid method called Artificial Neural Network with Simulated Annealing (ANN/SA), and Gene Expression Programming (GEP) had been built individually. ANN/SA has shown outstanding performance with an R-squared equal to 0.99 and root mean square error of 0.0028; hence, it has been used in the actuation process for magnetic field prediction.

Finally, to indicate the functionality of the system, a simple 1D PI actuation logic with $k_p = 3.25$ and $k_i = 0.01$ using a laser sensor had been successfully investigated. It first predicts the magnetic field using ANN/SA at the agent's current position provided by the laser sensor; then, regulates the current flowing through each coil till the agent settles at the final destination.

Acknowledgements

I would like to extend my deepest gratitude to my supervisor, Prof. Behrad Khamesee, for his invaluable advice, unwavering support, and patience during my Master's study. His immense knowledge and experience have encouraged me in my academic research and daily life. It was a great honor to work under his supervision.

I would like to extend my sincere thanks to Prof. William Melek and Prof. Christopher Nielsen for their valuable comments.

I am also grateful to Dr. Xiaodong Zhang and Dr. Ashkan Pourkand for their help and support during this work.

Lastly, I shall express my deepest gratitude to my family for providing unfailing support and constant encouragement in my study.

Table of Contents

List of Figures

x

List of Tables

Chapter 1

Introduction and literature review

In this chapter, various applications of magnetic actuators, also known as magnetic manipulators, will be discussed. Then, the advantages of the microsurgery field will be thoroughly explained. After explaining the motivation of this research, a review of related published literature will be presented. Ultimately, the contributions and the thesis organization are provided.

1.1 Introduction

Magnetic actuators have been implemented in various applications such as metal forming, where magnetic force generated by a fifteen-turn solenoid pushes a light metal to form the cellphone case [1]. Another exciting application is additive manufacturing using a 3D printer to produce magnetic materials while printing. The magnetic field is utilized to align the magnetic particles during the print process [2]. In another study, the strength of the levitation of a single iron-core coil(electromagnet) is utilized to measure the density of dense non-magnetic materials like glass [3]. Defect detection feasible by measuring the change in the eddy current produced by a coil is also a massive advantage of the magnetic actuators [4].

Moreover, magnetic actuators are used in micro-electro-mechanical systems (MEMSs) to actuate micro pumps [5]. Also, actuating two micro fingers made by soft magnetic materials to stably grasp a micro size material [6] and enabling an accurate pick-and-place process using a micro-robot agent [7] are other advantages of the magnetic actuators. Small force sensing [8], contactless delivery [9], and microsurgery [10] are a few other applications of this field. In particular, minimally invasive surgery (MIS) is a branch of the microsurgery field that might change the operational procedures in the medical field.

MIS has absorbed the attention of researchers and investors in the robotic field worldwide as it offers promising benefits like lower infection risk, fewer medical complications, and faster rehabilitation which are some of the core considerations of any surgical procedure [11]. Sub-millimeter agents manipulated wirelessly via magnetic field could potentially modernize the medical field [12]. The combination of bioengineering, robotics, image processing, mechanical and electrical engineering can replace the current devices in hospitals, sports centers, and medical clinics with safer alternatives. Newly designed equipment enables surgeons to access fragile organs of the human body like the eye, heart, and brain to perform more precise and less invasive operations in sanitized environments. It can also navigate capsules inside the body for targeted drug delivery purposes and provide harmless access to the parts that were not safely approachable previously. Eventually, this system will cause minor damage to the tissues to access the troubled organ, which will increase the rehabilitation pace [13].

Several research groups in the world focused their time and effort on developing a reliable and controllable system that is not harmful to the human body and can address the mentioned benefits. Magnetic manipulators seem to be the potential solution.

1.2 Literature Review

This section studies the literature on different manipulators fabricated through years to wirelessly provide a controlled actuation over microrobots to achieve a harmless manipulation environment.

Keuning and et al. developed a magnetic manipulator, shown in Figure 1-1, that moved a team of spherical paramagnetic particles inside water using four magnets. The particles had an average size of $100 \ \mu m$, and a microscopic image provided the current state of the particles. The water tank was a $10 \times 10 \times 5 \ mm$ cube inside the $20 \times 20 \ mm$ working space. The operation had been done only in a 2D region of interest that was normal to the camera view. This manipulation has been successfully conducted with an average error of $8.4 \ \mu m$ [14]. It utilized four air-core coils with a ten-millimeter

inner and a thirty-nine-millimeter outer radius of thirty millimeters long. Also, each coil had a resistance of twelve ohms and an inductance of twenty-five milli-henry.
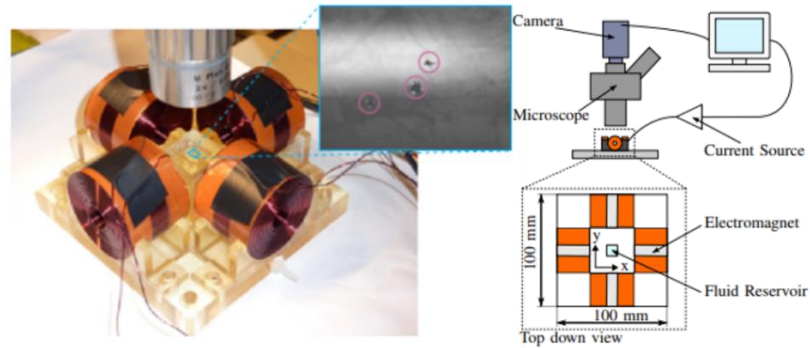
Figure 1-1: Magnetic system developed by Keuning and et al [14].

Air-core coils provide less magnetic field strength than iron-core ones; however, there is no general analytical model. Therefore, researchers implemented the Finite Element Method (FEM) to calculate the magnetic field values of an iron-core coil to manipulate heavier robots or increase the working space [15].

The enhancements were not restricted to the coil types and the magnetic field measurement techniques. Multiple research teams conducted projects on developing magnetic devices that had their unique response to the same magnetic field; consequently, each robot could be controlled individually over the same produced magnetic field [16][17]. Figure 1-2 shows four iron-core coils acting on a chamber containing an agent with four different materials at each layer. The magnetic field has been calculated by applying FEM, and each layer responded differently to the magnetic field. This work combines developments in both calculation and agent levels.
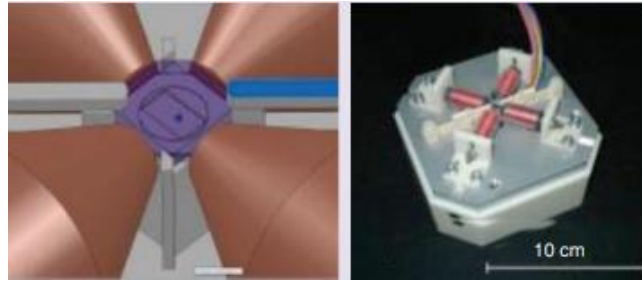
Figure 1-2: Four iron-core coils acting on a chamber [16]

Moving forward, OctoMag is another magnetic actuator developed to enhance retinal surgery; this device contains eight electromagnets to perform a 5 degree of freedom (5 DOF) -transition and orientation, also known as the state- via magnetic force and torque control. More precisely, this system captures the agent's state using two cameras and relates the state to the current that passes through each coil. By applying Maxwell laws, the current and state of the agent are related to the force and torque experienced by the agent.

Magnetic manipulation could eliminate the irreversible damage to the eye through the control constraints that could even respond appropriately to unpredicted issues such as patient movement [18]. Octomag also implemented a linear relationship of fields generated from each coil to calculate the contribution of each coil in the field. The region of interest of $20\ mm$ cube with the acuuracy of $2.9\ \mu m$ had been selected for the separate manipulation of two robots, made from Ni and CoNi. OctoMag simulated the field using FEM and then calibrated the simulated field with one known value measured from the actual coil. Octomag's coils are two hundred and ten millimeters long and nineteen millimeters thick, with a core diameter of forty-four millimeters individually. Each coil also produces eighty-nine milli-henry inductance with around one and a half ohms resistance.

Minimag was motivated by OctoMag, enabling 5 DOF inside a spherical working space surrounded by eight iron-core coils. This system also followed the same approach to calibrate the FEM simulations [19]. Figure 1-3 a and b illustrates these two systems. Another design consisted of eight metal-core

coils that tried to implement the same concept as the Octomag to navigate a capsule inside the stomach is shown in Figure 1-3 c, the magnetic actuator would control the point-to-point capsule endoscope movement and fixed-point rotation [20]. This system uses a rectangular coil instead of cylindrical, and its working space is a cone with a base of 220 mm and height of 140 mm.
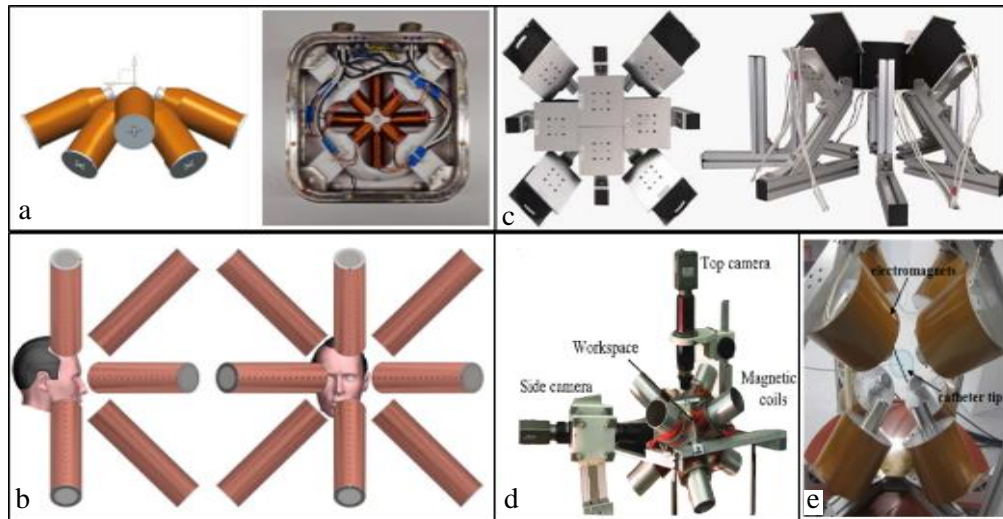
Figure 1-3: a) MiniMag [19] b) OctoMag [18] c) rectangular coil [20] d) replicable core [21] e) long core [22]

Researchers' enthusiasm had led them to investigate the possibility of independent motion of a team of robots in 3D space and the feasibility of path planning along arbitrary trajectories. Eight iron-core electromagnets aligned toward the same point had been used to manipulate robots inside the working area. These coils wound around a nonmagnetic core so the core part could be inserted and withdrawn for different scenarios [23].

Catheter positioning also is a massive advantage of the magnetic manipulators; the catheter guidance control and imaging (CGCI) systems use eight giant coils and have been implemented in the industrial size [24]. Recently T. Le and et al. have developed a manipulation system with a core longer than the coil length to navigate the catheter in a $128 \times 128 \times 128\ mm$ working space. Core length is almost

seventy percent longer than the coil, and it produces twenty times stronger fields than a similar air core coil. The core is a cylindrical iron with sixty-eight millimeters in diameter and two hundred and eighty millimeters in length. The coil is only a hundred and forty millimeters long with a thickness of seventy-two millimeters. Furthermore, three magnets made from NeFeB had been implemented in a tube to form the catheter [24].
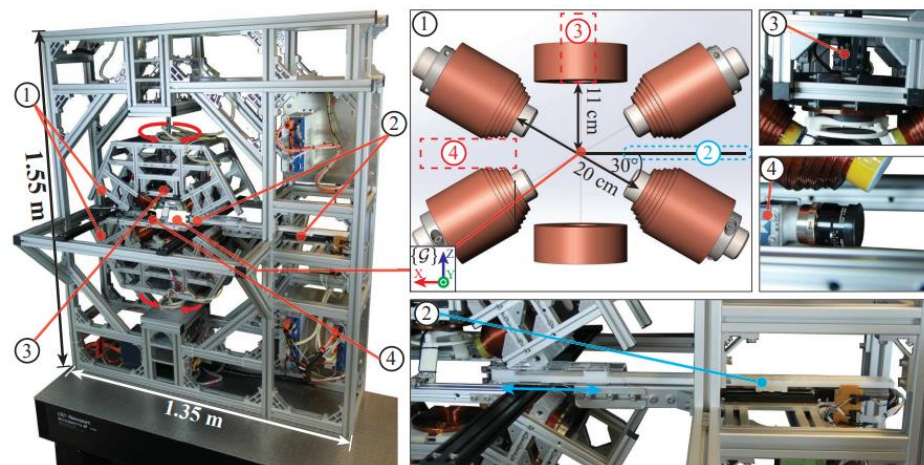
Figure 1-4: BigMag [25]

Moreover, BigMag, illustrated in Figure 1-4, has utilized six non-stationary coils to navigate a catheter made from a permanent magnet disk in a 2D space shaped like the human lounge. Each coil at BigMag has an inner diameter of forty-five millimeters and an outer diameter that varies along with the coil's height from fifty-six to hundred and two millimeters plus the resistance of about four ohms. Ultimately, the length of each coil and its core are a hundred twenty and a hundred eighty millimeters, respectively.

Another system that implemented catheter control through the human lounge was developed by Edelmann et al., where eight coils were used to control the catheter in a cubic workspace [26]. Table 1-1 includes all the reported aspects of the mentioned systems and their coil specifications.

Table 1-1: Manipulator reported specifications

	air coil	Minimag	octomag	rectangle coil	replaceable core	Long core	BigMag
inner diameter mm	10	-	44	30	51	68	45
outer diameter mm	39	-	63	60	-	140	56-102
Coil length mm	30	-	130	120	32	170	120
Core length mm	-	-	-	-	-	279.31	180
Maximum current A	0.8	6	15	-	19	-	8
Resistance Ω	12	-	1.3	1.5	0.4	4.1	4.2
number of turns	1680	-	-	-	140	-	-
Robot material	paramagnetic	CoN	Ni/CoNi	-	NdFeB	NdFeB	-
number of coils	4	8	8	8	8	8	6
maximum field value mT	-	20	15	-	8.3	-	-

1.3 Motivation and Contributions

The goal is to develop a magnetic manipulator that can remotely navigate a robot inside a working space. The robot can be equipped with specialized agents to be used in vast applications from manufacturing, micro-assembly, and medical fields. Magnetic manipulation has advantages over conventional manipulators because it is wireless, safe, reliable, repeatable, and for medical applications,

minimally invasive. Since the design manipulator will be used for research purposes, designing a framework that works in different scenarios is essential.

These scenarios can be conducted based on different coil sizes placed at different distances; therefore, the framework should accommodate various dimensions as the working space. The designed system also must operate in a safe environment, where there is no access to the equipment operating in high voltage or carrying a high amount of current-consuming more than 100 watts or 40 volts.

The complexity of composing a magnetic manipulator has allowed exploring different areas. These opportunities paved the way to add some valuable contributions to this project. The goal of this research is to design a manipulator using electromagnets for medical application; the contributions have been listed in the following:

- Parametrize the geometrical constraint and its relationship with the coil's outer diameter.
- Optimize the coil dimensions with respect to two objectives, power consumption and axial force strength.
- Replacing FEM with Artificial Intelligence to predict the magnetic field of the manufactured coil.
- Design and fabrication of a unique manipulator with nine coils.

1.4 Thesis Organization

Chapter 1 presents the introduction and motivations of the thesis. Afterward, a detailed review of magnetic manipulation is presented, the specifications of each system, and its purpose. Consequently, it demonstrates the contributions and thesis organization.

Chapter 2 discusses the modeling of the magnetic field, force and torque calculations, superposition implementation, the Finite element method, and the homogeneous transformations, which will be used in Chapter 4 and Chapter 6. It also presents proof of a minimum number of coils required for manipulation.

Chapter 3 comprehensively explains the regression algorithms, data processing, and performance measurements utilized for magnetic field prediction. Artificial Neural Network, Artificial Neural Network with simulated Annealing, and Genetic Expression Programming are discussed. The provided information in this chapter will be helpful reading Chapter 6.

Chapter 4 introduces the parametrizing of the working space's geometric constraints considering the coils' outer diameter; then, it describes formulating the coil winding process for coil dimension modeling. It also explains Fabry Factore and investigates the effect of core on the magnetic field strength. The properties of the coil are also formulated in this chapter. Ultimately, the methodology behind the framework design is presented.

Chapter 5 outlines the electrical circuits and equipment selection followed by safety implementations.

Chapter 6 describes the experiments conducted for inductance calculation and discusses the regression results and algorithms' performance. Moreover, it describes the actuation logic for agent manipulation.

Chapter 7 concludes the research and suggests future work.

Chapter 2

Modeling the electromagnetic field

Electromagnets (coils) are the major components of the magnetic manipulator, and hence, they should be designed properly to optimize the system's performance. Expressing the behavior of an electromagnetic system is based on the accurate modeling of the magnetic field since the magnetic field will determine the amount of force and torque applied to an agent in the working space. The axial force caused by the calculated magnetic field also is a critical value in the coil's dimension optimization process. In this chapter, the analytical model used to express the magnetic field for an air-core coil will be expressed. This model will be used to validate the iron-core effect in Chapter 4. Next, a brief explanation of the FEM approach to calculate the magnetic field of an iron-core coil is expressed.

Consequently, the force and torque -the wrench- modeling for a known magnetic field and a magnetic dipole of an agent will be presented. Once the magnetic field and wrench modeling is completed, the proof of requiring at least eight coils for achieving 5 DOF control will be explained. Finally, the principles of the homogenous transformation matrix will be discussed.

2.1 The magnetic field of an electromagnet

In order to calculate the magnetic field, the relationship between the current passing through a coil and the coil's dimensions should be formulated. The biot-savart law expresses this relationship and enables magnetic field calculation [27]. By applying this rule to a single wire ring located on the yz plane and centered on the origin of the coordinate system with a radius of r carrying I amount of

current, the magnetic field value can be calculated. The magnetic field is reported in Tesla, T. Figure 2-1 illustrates the single ring with mentioned conditions.
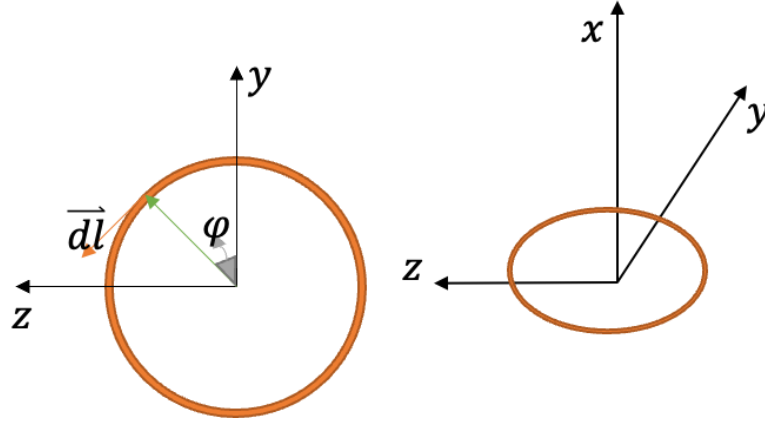
Figure 2-1: Single ring of wire

$$B = \frac{\mu_0}{4\pi} \int_C \frac{I\overrightarrow{dl} \times \overrightarrow{r'}}{|\overrightarrow{r'}|^3} \quad [28] \tag{1}$$

$$\overrightarrow{dl} = r\left(0\hat{\imath} - \sin(\varphi)\hat{\jmath} + \cos(\varphi)\hat{k}\right)d\varphi \tag{2}$$

$$\vec{P} = P_x\hat{\imath} + P_y\hat{\jmath} + P_z\hat{k} \tag{3}$$

$$\vec{r} = 0\hat{\imath} + r\cos(\varphi)\hat{\jmath} + r\sin(\varphi)\hat{k} \tag{4}$$

$$\overrightarrow{r'} = \vec{P} - \vec{r} = P_x\hat{\imath} + \left(P_y - r\cos(\varphi)\right)\hat{\jmath} + \left(P_z - r\sin(\varphi)\right)\hat{k} \tag{5}$$

where $0 \leq \varphi \leq 2\pi$. Applying equations (2) to (5) into the equation (1) :

$$B(x,y,z) = \frac{\mu_0 Ir}{4\pi} \int_0^{2\pi} \frac{\begin{bmatrix} 0 \\ -\sin(\varphi) \\ \cos(\varphi) \end{bmatrix} \times \begin{bmatrix} P_x \\ P_y - r\cos(\varphi) \\ P_z - r\sin(\varphi) \end{bmatrix}}{\left[P_x^2 + \left(P_y - r\cos(\varphi)\right)^2 + \left(P_z - r\sin(\varphi)\right)^2\right]^{3/2}} d\varphi \tag{6}$$

where μ_o is the magnetic permeability of the free space equal to $4\pi \times 10^{-7}$ Henry per meter. To calculate the magnetic field of a multilayer cylindrical air-core coil, the integration can be expanded

11

over the volume of the coil carrying a current density of J, in Amp.m^{-2}, with N number of turns [29].

Figure 2-2 represents the multilayer air-core coil with an inner radius of r_{in}, outer radius of r_{out} and length of L.
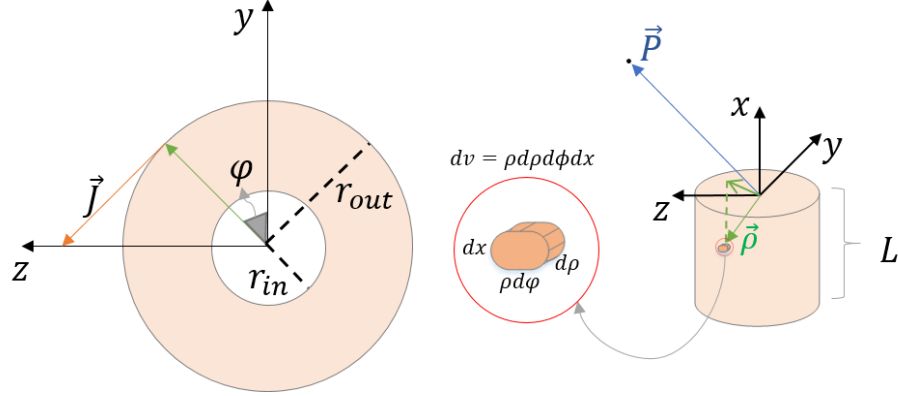
Figure 2-2: An air-core Coil

$$\vec{J} = 0\hat{\imath} - |J|\sin(\varphi)\,\hat{\jmath} + |J|\cos(\varphi)\,\hat{k} \tag{7}$$

$$A = (r_{out} - r_{in})L \tag{8}$$

$$|J| = \frac{IN}{A} \tag{9}$$

$$dv = \rho\, d\rho\, d\phi\, dx \tag{10}$$

By applying modified (3) to (5), where r is substituted with ρ, and implementing (7) to (10):

$$B = \frac{\mu_0}{4\pi} \iiint_v \frac{\vec{J}\times\vec{r'}}{|\vec{r'}|^3}\, dv \,[30]$$

$$B(x,y,z) = \frac{\mu_0}{4\pi} \int_{-L}^{0} \int_{0}^{2\pi} \int_{r_{in}}^{r_{out}} \frac{\begin{bmatrix} 0 \\ -|J|\sin(\varphi) \\ |J|\cos(\varphi) \end{bmatrix} \times \begin{bmatrix} P_x \\ P_y - \rho\cos(\varphi) \\ P_z - \rho\sin(\varphi) \end{bmatrix}}{\left[P_x^2 + \left(P_y - \rho\cos(\varphi)\right)^2 + \left(P_z - \rho\sin(\varphi)\right)^2 \right]^{3/2}} \rho\, d\rho\, d\phi\, dx \tag{11}$$

12

So far, the magnetic field of an air-core coil has been modeled. However, a high-performance soft-magnetic material can be inserted inside the coil to increase the magnetic field produced by a coil [31]. The Finite Element Method (FEM) can be used to calculate a coil with a non-air core. In this project, Ansys Maxwell 2020 is utilized for FEM modeling.

FEM analysis solves the magnetic field by using Maxwell equations; it describes the magnetic vector potential (A) at each node. Then by considering some boundary conditions such as the Coulomb gauge, meaning that $\nabla \cdot A = 0$, and $\nabla^2 A = \mu J$, and magnetic flux density, H, solve the $\nabla \times A = B$ [32][33]. Mesh size, error of convergence, and the size of the vacuum space around the coil, where J is equal to zero, are essential parameters employing Ansys Maxwell. This software has a library of different materials with associated magnetic properties, making the FEM modeling easily applicable for the research.

2.2 Force and Torque modeling

Modeling the force and torque, called wrench together, caused by a coil is crucial since it will first predict the wrench value experienced by an agent for control purposes. Second, it will indicate the minimum number of coils required for five degrees of freedom controllability over the working space, shown in Figs. Third, it will be one of the optimization objectives for coil dimension optimization. Some efforts for 2D force-based control under restrictions like using nonmagnetic forces such as gravity to stabilize the system inside a small working space with only three coils had been made [34]. However, the rotation of the coil was not controlled in this study; therefore, the 3D state control method with the minimum possible coils was investigated [21].
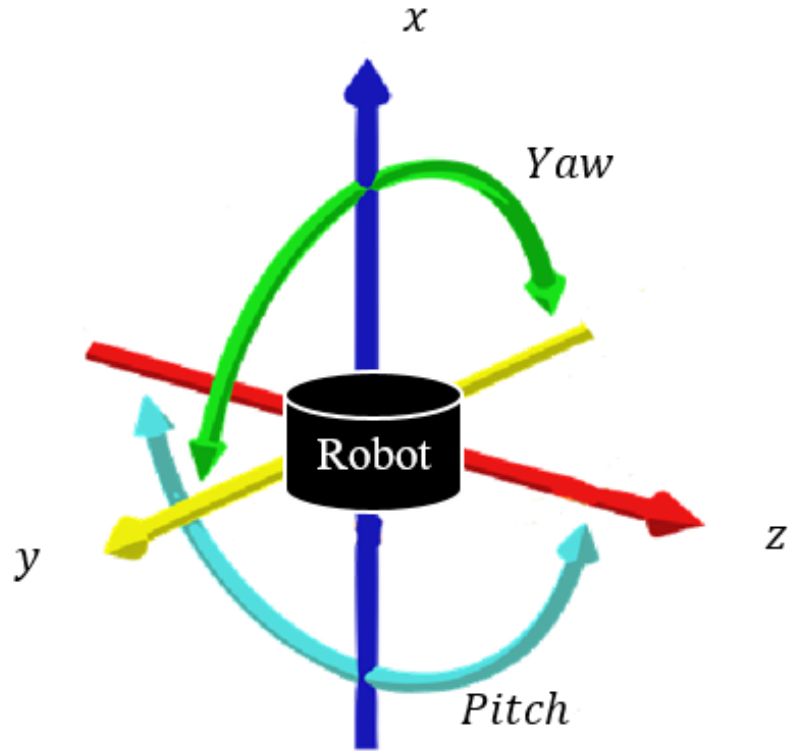
Figure 2-3: Five degrees of freedom of a robot with magnetic dipole moment along the x-axis

2.2.1 Magnetic manipulation background

As mentioned before, Maxwell's equations have been used to describe the quasi-static magnetic field used for magnetic manipulation [35].

$$\vec{\nabla}.\vec{B} = 0 \tag{12}$$

$$\vec{\nabla} \times \vec{B} = \mu_0 \vec{J} \tag{13}$$

The force and torque acting on an object with the dipole moment of $\vec{m}$ exposed to a magnetic field also can be described as:

$$\vec{F} = (\vec{m}.\vec{\nabla})\vec{B} \tag{14}$$

$$\vec{\tau} = \vec{m} \times \vec{B} \tag{15}$$

14

By developing (14):

$$\vec{F} = \left(m_x \frac{\delta B_x}{\delta x} + m_y \frac{\delta B_x}{\delta y} + m_z \frac{\delta B_x}{\delta z} \right) \hat{\imath} + \left(m_x \frac{\delta B_y}{\delta x} + m_y \frac{\delta B_y}{\delta y} + m_z \frac{\delta B_y}{\delta z} \right) \hat{\jmath}$$
$$+ \left(m_x \frac{\delta B_z}{\delta x} + m_y \frac{\delta B_z}{\delta y} + m_z \frac{\delta B_z}{\delta z} \right) \hat{k} \tag{16}$$

One can expand (12) and (13) to simplify (16):

$$\vec{\nabla}.\vec{B} = \frac{\delta B_x}{\delta x} + \frac{\delta B_y}{\delta y} + \frac{\delta B_z}{\delta z} = 0$$

$$\frac{\delta B_z}{\delta z} = -(\frac{\delta B_x}{\delta x} + \frac{\delta B_y}{\delta y}) \tag{17}$$

Since there is no current following through the working space, $J = 0$:

$$\vec{\nabla} \times \vec{B} = \begin{vmatrix} \hat{\imath} & \hat{\jmath} & \hat{k} \\ \frac{\delta}{\delta x} & \frac{\delta}{\delta y} & \frac{\delta}{\delta z} \\ B_x & B_y & B_z \end{vmatrix} = 0 \tag{18}$$

Therefore:

$$\frac{\delta B_z}{\delta y} = \frac{\delta B_y}{\delta z} \tag{19}$$

$$\frac{\delta B_z}{\delta x} = \frac{\delta B_x}{\delta z} \tag{20}$$

$$\frac{\delta B_y}{\delta x} = \frac{\delta B_x}{\delta y} \tag{21}$$

By applying (17) to (21) equations into (16) and transferring it into the matrix form:

15

$$\vec{F} = \begin{bmatrix} m_x & m_y & m_z & 0 & 0 \\ 0 & m_x & 0 & m_y & m_z \\ -m_z & 0 & m_x & -m_z & m_y \end{bmatrix}_{3\times5} \begin{bmatrix} \dfrac{\delta B_x}{\delta x} \\[4pt] \dfrac{\delta B_x}{\delta y} \\[4pt] \dfrac{\delta B_x}{\delta z} \\[4pt] \dfrac{\delta B_y}{\delta y} \\[4pt] \dfrac{\delta B_y}{\delta z} \end{bmatrix}_{5\times1} = h(\vec{m})g(\vec{\nabla}\vec{B}^T) \tag{22}$$

where h and g are functions that transfer $\vec{m}$ to 3×5 and field's gradient to 5×1 matrices, respectively.

Furthermore, using the skew-symmetric matrix function, symbolized as $S(.)$, (15) can be written as:

$$\vec{\tau} = \begin{bmatrix} 0 & -m_z & m_y \\ m_z & 0 & -m_x \\ -m_y & m_x & 0 \end{bmatrix}_{3\times3} \begin{bmatrix} B_x \\ B_y \\ B_z \end{bmatrix}_{3\times1} = S(\vec{m})B \tag{23}$$

By combining (22) and (23), the wrench effecting on dipole will be developed:

$$\vec{W} = \begin{bmatrix} \vec{\tau} \\ \vec{F} \end{bmatrix}_{6\times1} = \begin{bmatrix} S(\vec{m})_{3\times3} & 0_{3\times5} \\ 0_{3\times3} & h(\vec{m})_{3\times5} \end{bmatrix}_{6\times8} \begin{bmatrix} \overrightarrow{B_{3\times1}} \\ g(\vec{\nabla}\vec{B}^T)_{5\times1} \end{bmatrix}_{8\times1} \tag{24}$$

As (24) indicates, the mechanical 6 DOF is the function of eight magnetic DOF. Equation (13) shows that the magnetic field and its gradient are related to the current density, which is linearly related to the current going through each coil. Therefore, the wrench affecting the object inside the working space can be further expanded for each point, shown by letter p, on the working space for N coils, minimum of eight.

$$\overrightarrow{B}(p, I) = \vec{B}(p)I \tag{25}$$

$$G(p, I) = g(\vec{\nabla}\vec{B}(p, I)^T) = g(\vec{\nabla}\vec{B}(p)^T)I = G(p)I \tag{26}$$

By applying (25) and (26) into (24) and modifying it for N coils:

16

$$\vec{W} = \begin{bmatrix} \vec{\tau} \\ \vec{F} \end{bmatrix}_{6\times 1} = \begin{bmatrix} S(\vec{m})_{3\times 3} & 0_{3\times 5} \\ 0_{3\times 3} & h(\vec{m})_{3\times 5} \end{bmatrix}_{6\times 8} \begin{bmatrix} \vec{B}(p) \\ G(p) \end{bmatrix}_{8\times N} I_{N\times 1} \qquad (27)$$

Equation (27) relates the current of an individual coil and its magnetic field plus the associated gradients of unit current to the wrench experienced by an agent with the known magnetic dipole at any point in the working space. It is worth mentioning that the physical implementation of (27) exhibits a singularity around the dipole direction of the agent; accordingly, the system can reach only 5DOF in practice.

Furthermore, equation (27) requires $\vec{B}(p)$ and $G(p)$ values of each coil at the Global Coordinate System (GCS); therefore, the desired point at GCS needs to be transferred to the Local Coordinate System (LCS) of each coil. Then, the calculated $\vec{B}(p_{LCS})$ and $G(p_{LCS})$ should be transferred back to the GCS system.

2.2.2 Homogeneous transformation

In order to transfer a vector from GSC to LSC or vice versa, the homogenous transformation matrix concept had been implemented.
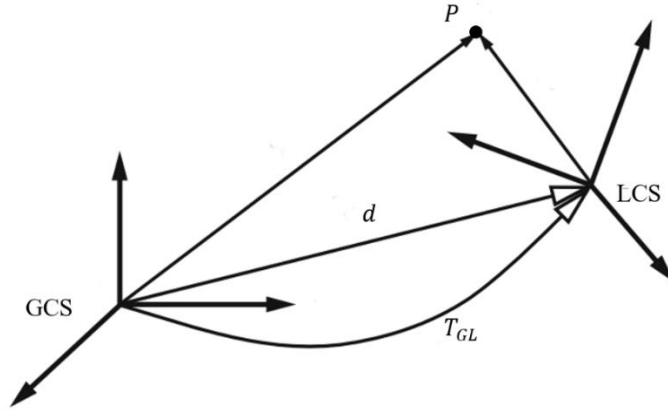
Figure 2-4: Global and local frames[36]

As indicated in Figure 2-4 [36], point P can be mapped from global coordinate to local one if the distance between the origin of two coordinates, d, and the rotation, R, are known. T_{GL} is the homogeneous transformation that represents LCS relative to GCS.

$$T_{GL} = \begin{bmatrix} R_{GL} & d \\ 0_{3\times1} & 1 \end{bmatrix} \tag{28}$$

Equation (28) indicates that homogeneous transformation is a 4×4 matrix. The bottom row consists of three zeros and a one to simplify matrix operations. The homogeneous transformation matrix is a member of the Special Euclidean group, SE(3) set; the rotational matrix is also a member of the Special Orthogonal group, SO(3) set; both matrices satisfy similar properties by being a member of these two sets [37].

For example, each matrix has an inverse such that the matrix times its inverse is the identity matrix of the same size in the associated set. The product of two rotational or transformation matrices also is a rotational or transformation matrix. Moreover, matrix multiplication is associative but not commutative. Since there are several ways to rotate a frame, it is better to use an order to keep track of the rotations. In this project, the YZY Euler angle is utilized.

In order to move back from LCS to GCS, the inverse of the T_{GL} is required:

$$T_{LG} = T_{GL}^{-1} = \begin{bmatrix} R_{GL}^{-1} & -R_{GL}^{-1}d \\ 0_{3\times1} & 1 \end{bmatrix} \tag{29}$$

Once the transformations matrix and its inverse is developed, the $\vec{B}(p)$ and $G(p)$ in equations (25) and (26) can be individually developed using FEM or measured experimentally by a gausses meter and then transferred to GCS.

Chapter 3

Artificial Intelligence

This chapter describes why Artificial Intelligence has been chosen over FEM for the experiment. Moreover, it describes the principles of the three models, Artificial Neural Network (ANN), a hybrid method called Artificial Neural Network with Simulated Annealing (ANN/SA), and Gene Expression Programming (GEP). It also discusses the data processing and performance evaluation methods.

3.1 AI, an alternative for FEM simulations

Measuring the actual magnetic field values produced by a fabricated coil could be an alternative for the simulated magnetic field values produced by FEM. In order to measure the magnetic field and required gradient components at each point required for (27), $\vec{B}(p)$ and $G(p)$, FEM method has been used. In this work also Ansys Maxwell 2020 used to calculate the magnetic field caused by a coil energized by a unit current. However, there are some disadvantages to using the FEM approach that could be eliminated using AI regression algorithms.

As previously mentioned, FEM approximates the magnetic field by solving for the potential vector at each node and minimizes the error at each iteration till it converges toward the desired error value. Produced results are also sensitive to the vacuum space size and the mesh size used during simulation. In order to get reliable results, especially with 3D meshing, a higher number of nodes meaning smaller mesh size and a more significant vacuum area, are required, which the modeling computationally complex. The FEM can also not precisely capture the human errors involved in the core manufacturing and coil winding processes.

Therefore, the FEM results are traditionally scaled by a scalar to overcome the stated issues. The scalar is the division of the measured magnetic field of a known point by the corresponding magnetic

value in the simulation. Figure 3-1 indicates the x component of the magnetic field over a similar line

for an iron-core coil with different values of a material property symbolized as μ for iron (will be

defined later). Increasing the μ value should result in higher magnetic field values; however, it is seen

that FEM results in some cases decrease while μ is increasing. This Figure indicates that for 3D

simulation of a single coil, the FEM results even do not follow the physical knowledge.
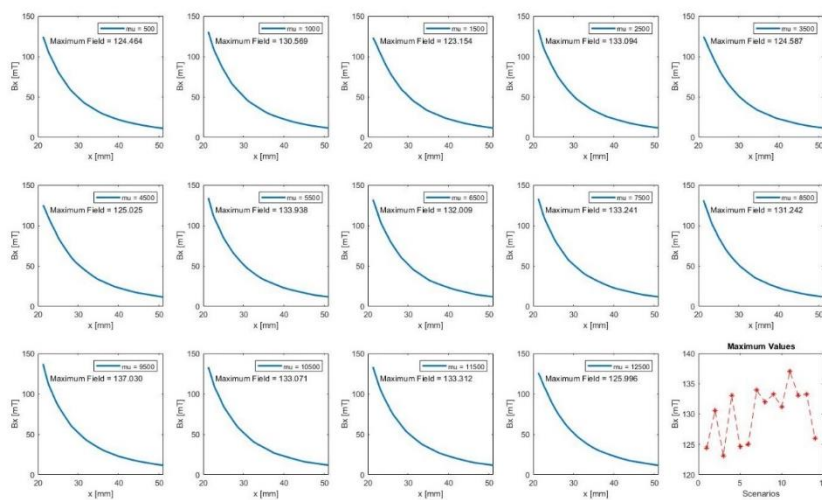
Figure 3-1: FEM results in 3D for μ ranges from 500 to 12500

The issues associated with the FEM encourage finding an alternative for experimental

implementations. The magnetic field components of a coil can be measured using a gauss meter to

develop regression models to predict the magnetic field values caused by the actual coil. The data set

can be measured over a shallow grid since the coils are designed to work in their almost linear operation

range. Moreover, regression models can capture the general relationship between data points; therefore,

a high-resolution grid for data collection is not required. Ultimately, a regression model is suggested as

a replacement for FEM, and it should not add a cumbersome effort to the implementation process;

hence, a shallow grid is time-efficient.

3.2 Regression models

Regression is a technique where an algorithm approximates the true function to map inputs of a data set to the desired output:

$$y = f(x, \beta) + e \tag{30}$$

where y is the actual value which depends on the input x, the unknown parameter β and the modeling additive error, e. In the absence of an analytical model, researchers try to approximate the function $f(x, \beta)$ by using the collected data set to explain the system's behavior. In this research, inputs are the position coordinate of the agent in the region of interest, and the output is magnetic field parameters. Three algorithms have been implemented for the approximation; Artificial Neural Network (ANN), a hybrid method called Artificial Neural Network with Simulated Annealing (ANN/SA), and Gene Expression Programming (GEP).

3.2.1 Artificial Neural Network (ANN)

The artificial neural network is a deep learning approach, a subfield of machine learning, where the structure of the human brain inspires the foundation of the algorithm [38], Figure 3-2 is a simple biological illustration of the neuron [39], and Table 3-1 is the ANN equivalent terminology of it [40]. The ANN uses training data to recognize the patterns and predict the outputs for a new set of similar data [41]. The training data is fed to the network as an input layer; then, it moves along channels through hidden layers, which are the core processing units of the network, to the output layer. Figure 3-3 indicates the general structure of a network.
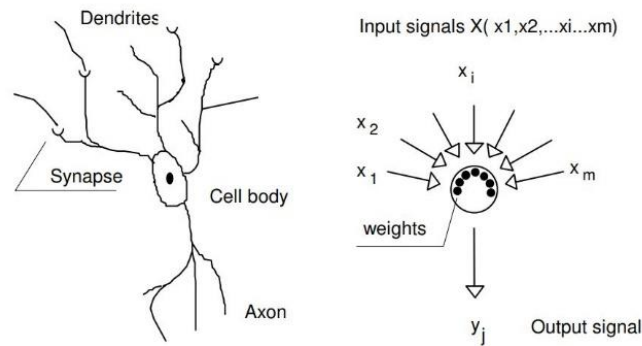
Figure 3-2: Brain cell [39]

Each channel is assigned to a number known as weight that scales the neuron from the previous layer and feeds it to the neuron in the next layer. All the channels toward a particular neuron will be added together; then, another value known as bias or interception point is added to this equation. Finally, an activation function will be applied to the neuron before it leaves toward the next layer through its channels. For most regression problems, the outer layer is only a summation of the last layer's neuron values multiplied by their associated weights plus the interception point without any activation matrix. Figure 3-4 illustrates the scaling, bias, and activation function over one neuron only; this process is known as forward propagation [42]. It is worth mentioning that forward propagation starts with the initial values provided by the user.

Table 3-1: ANN terminology

Biological	ANN
Dendrites	Input
Neuron/ Cell body	Node/Unit/Cell/Element
Synapse/Axon terminals	Connection/Edge/Link/ Channel
Synaptic efficiency	Connection strength/Weight
Firing frequency/ Axon	Node output
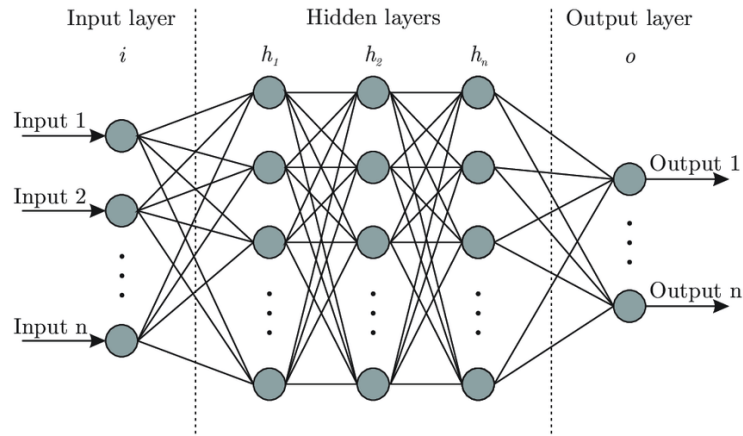
Figure 3-3: Artificial neural network structure
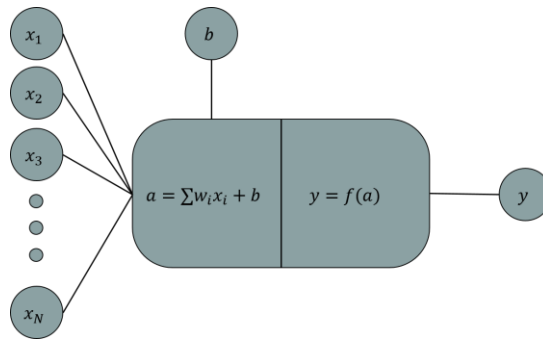
Figure 3-4: Operations in one neuron

ANN can be implemented utilizing the for loops or the matrix multiplication; however, matrix operations are computationally more efficient than loops. In order to develop a matrix form of the forward propagation process, first, a proper formatting of weights, biases, and neuron values of each layer is required. The weight associated with the channel that connects the jth neuron of the layer l to the ith element of the next layer will be shown as $w_{ji}^{(l)}$; the first number in the subscript is the neuron that channel leaves from, and the second one is where it lands; the superscript also refers to the layer

23

that the channel roots from, for example, $w_{52}^{(3)}$ connects the fifth neuron of the third layer to the second neuron of the fourth layer. The total number of layers and inputs indicated by L and m, respectively.

$$\begin{bmatrix} y_1^{(l+1)} \\ y_2^{(l+1)} \\ \vdots \\ y_n^{(l+1)} \end{bmatrix}_{n \times 1} = f\left(\begin{bmatrix} a_1^{(l+1)} \\ a_2^{(l+1)} \\ \vdots \\ a_n^{(l+1)} \end{bmatrix}_{n \times 1}\right) = \begin{bmatrix} w_{11}^{(l)} & w_{21}^{(l)} & & w_{k1}^{(l)} \\ w_{12}^{(l)} & w_{22}^{(l)} & \ddots & w_{k2}^{(l)} \\ \vdots & \vdots & & \vdots \\ w_{1n}^{(l)} & w_{2n}^{(l)} & & w_{kn}^{(l)} \end{bmatrix}_{n \times k} \begin{bmatrix} x_1^{(l)} \\ x_2^{(l)} \\ \vdots \\ x_k^{(l)} \end{bmatrix}_{k \times 1} + \begin{bmatrix} b_1^{(l)} \\ b_1^{(l)} \\ \vdots \\ b_n^{(l)} \end{bmatrix}_{n \times 1} \tag{31}$$

Where n and k are the number of neurons at the $l+1$ and the l layers, respectively. The weight matrix also can be shown as W^l.

This process would not individually train the network; the weights associated with the channels will be updated with respect to the error of last layer prediction and actual value, δ [43]. The weight adjustment process will be done through backpropagation, mainly using the gradient descent approach[40]. This process has been illustrated in Figure 3-5 for one neuron.
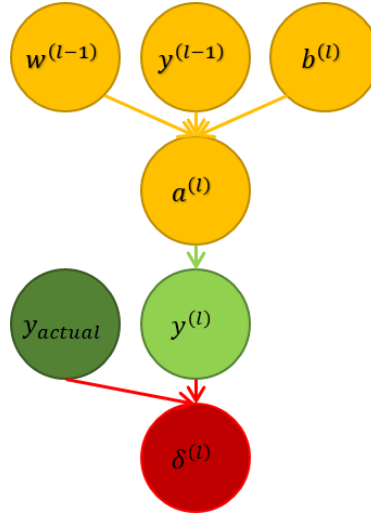
Figure 3-5: Backpropagation for one neuron

$$\delta^{(L)} = \left(y_{actual} - y^{(L)}\right)^2 \tag{32}$$

$$a^{(l)} = w^{(l-1)}y^{(l-1)} + b^{(l)} \tag{33}$$

24

$$y^{(l)} = f\big(a^{(l)}\big) \tag{34}$$

$$\frac{\partial \delta^{(l)}}{\partial w^{(l-1)}} = \frac{\partial a^{(l)}}{\partial w^{(l-1)}} \frac{\partial y^{(l)}}{\partial a^{(l)}} \frac{\partial \delta^{(l)}}{\partial y^{(l)}} = 2[y^{(l-1)} f'\big(a^{(l)}\big)\big(y_{actual} - y^{(L)}\big)] \tag{35}$$

$$\frac{\partial \delta^{(l)}}{\partial b^{(l)}} = \frac{\partial a^{(l)}}{\partial b^{(l)}} \frac{\partial y^{(l)}}{\partial a^{(l)}} \frac{\partial \delta^{(l)}}{\partial y^{(l)}} = 2[f'\big(a^{(l)}\big)\big(y_{actual} - y^{(L)}\big)] \tag{36}$$

$$w^{(l-1)} = w^{(l-1)} - \alpha \frac{\partial \delta^{(l)}}{\partial w^{(l-1)}} \tag{37}$$

$$b^{(l)} = b^{(l)} - \alpha \frac{\partial \delta^{(l)}}{\partial b^{(l)}} \tag{38}$$

Where α is called the learning rate, this process will be applied to all the neurons, and the adjusted W between the layers will be used for the next iteration. The training can be stopped after a certain number of iterations or once the cost function has not changed drastically. Figure 3-6 illustrates the entire training process [41].
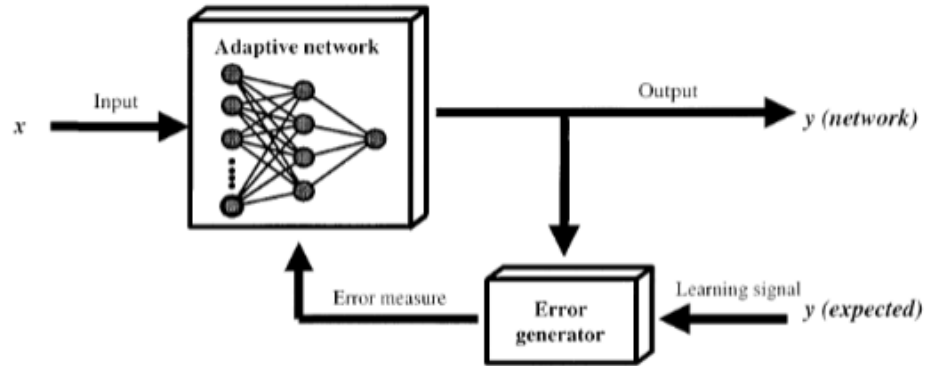
Figure 3-6: ANN training process [41]

3.2.2 Artificial neural network with simulated annealing

The assigned initial weights and biases affect ANN results for the first iteration of the feedforward process since it specifies the start of the cost function convergence. Some initial values like using the same weights will result in a local minimum for the cost function. Therefore, it is beneficial to develop a method that can produce initial weights and biases that increase the probability of reaching the global minimum and increase the learning pace of the network.
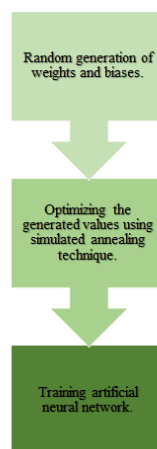
Figure 3-7: ANN/SA process

As indicated in Figure 3-7, the hybrid simulated annealing-artificial neural network method optimizes the randomly generated initial weights and biases values; then, it starts the network training process. The thermomechanical annealing process inspired the optimization of random values [44]. The metal will be heated to a higher temperature and cooled down, resulting in a variation in the metal's atomic structure and material properties. The atomic structure and the temperature of the metal will be related together, and if the temperature drops slowly, it can be related to the energy change of the metal [45]. This method was used to optimize nonlinear functions involving multiple local minimums, and it uses the Metropolis algorithm to simulate the annealing process [46]. Since it is not a greedy process, the probability of reaching a local minimum is considerably low.

26

During the training process, the SA will adjust the weights randomly, considering the algorithm's temperature change and evaluating the network's accuracy; once the accuracy has been calculated, the Metropolis algorithm would decide whether the created solution is acceptable. Equation (39) evaluates the probability of acceptance (P_a):

$$P_a(\Delta E, y) = \begin{cases} e^{-\frac{k\Delta E}{y}} & \Delta E > 0 \\ 1 & \Delta E \leq 0 \end{cases} \tag{39}$$

Where ΔE is the error between the new solution and current solution, y is the current temperature, and k is the acceptance constant, based on the range of weights, biases, and inputs. As (39) indicates, the algorithm will frequently be accepting new results at high temperatures but becomes more selective at the lower ones [47]. Figure 3-8 illustrates three types of cooling schedules that can be used [48].
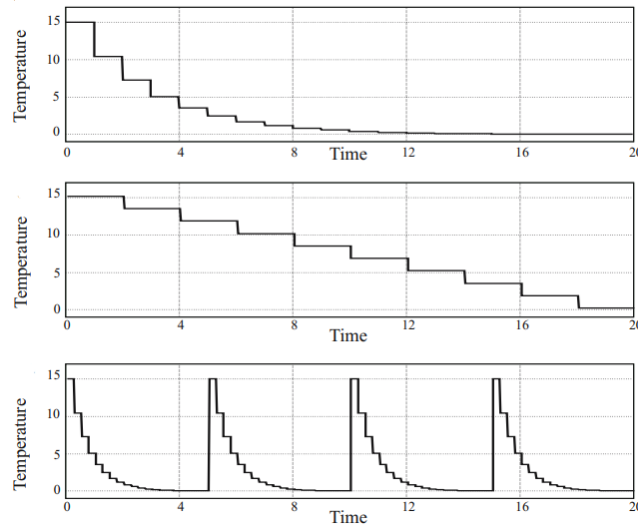
Figure 3-8: Top) Exponential cooling, Middle) Linear cooling Bottom) Temperature cycling [48]

In order to calculate the temperature at each state using the temperature cycling method, the following equations should be implemented. It first takes a series of $n \in [1, N]$ scenarios for temperature:

$$x[n + 1] = \rho x[n] \tag{40}$$

Where the total number of temperatures is N, the starting temperature is $x[1]$, the final temperature is $x[N]$, and cooling constant is ρ presented by:

$$\rho = e^{\log\left(\frac{(N-1)x[N]}{x[1]}\right)} \tag{41}$$

If the number of cycles before each optimization is expressed as M and the temperature assigned to the simulated annealing indicated by $y[n]$, the schedule of the cooling process can be modeled as:

$$y[n] = \sum_{m=0}^{M-1} x[n - mN] \tag{42}$$

Ultimately, the weight preparation of the temperature using the same formatting described at 3.2.1 can be formulated as:

$$w_{ij}^l[n + 1] = \gamma(1 - \lambda)w_{ij}^l[n] + \lambda u[n] - 0.5\,\lambda \tag{43}$$

where u is a random variable that is uniformly distributed and takes values between $[0, 1)$, γ is a value equal to 20 or 30, and λ is the perturbation ratio:

$$\lambda = \frac{y[n]}{x[1]} \tag{44}$$

3.2.3 Gene Expression Programming

Gene expression programming (GEP) belongs to a wilder set of genetic algorithms, a subset of evolutionary algorithms [49]. In this set, the algorithm uses populations of individuals and, based on the fitness, selects the individuals with high performance. Selected ones will be introduced to the genetic variation of one or more genetic operators. GEP benefits from the linear strings of fixed length encoded individuals, also known as genome [50]. Genomes are expressed as nonlinear entities of different sizes and shapes, forming simple diagram representations or expression trees (ETs) [51].

Each gene has a head and a tail size, taking operational functions or a feature input from the provided functions and features. The head size affects the width, and the tail influences the ET depth associated with each gene.

As Figure 3-9 a [52] indicates, the approximation randomly initializes the first population and develops ET expressions. Once the fitness accuracy of chromosomes has been calculated, those with a higher performance than a particular accuracy value will be moved to the next population. This population will add several newly generated chromosomes and continue the evaluation till the desired accuracy is achieved, or the performance has not increased considerably [53].
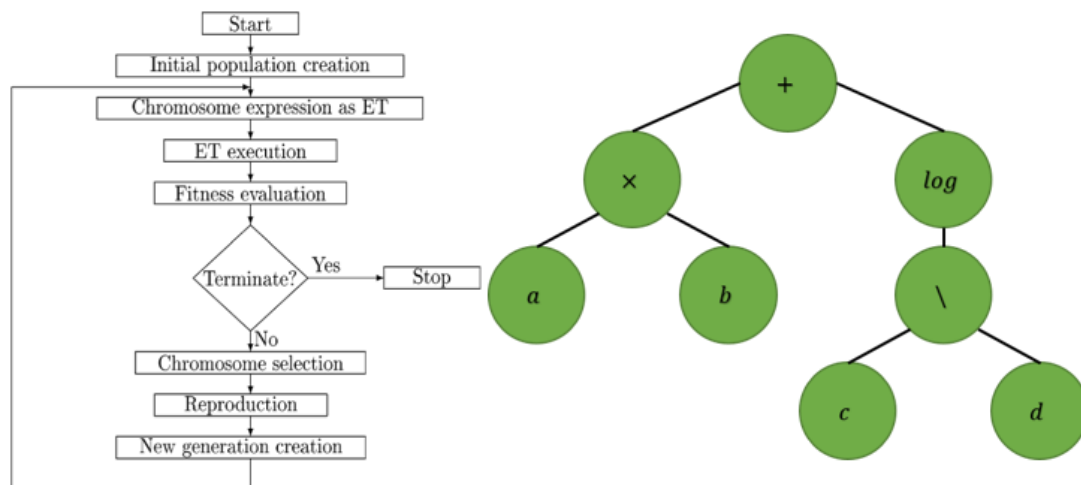
Figure 3-9: a) GEP algorithm [52] b) ET representation of the (45)

Figure 3-9 b represents a single chromosome with one gene and a head size of three in the ET format. This figure is the ET representation of the equation (45) where $a,b,c,$ and d are the features of an imaginary data set. As can be seen, increasing the number of genes will result in a more complex expression and computationally more expensive algorithms[54]. Population size also directly affects computation time as the performance of each chromosome needs to be evaluated; however, the natural

selection of highly valued chromosomes and moving them to the next population allows lower

population size; hence, faster algorithms.

$$(a \times b) + \log^{\frac{c}{d}} \tag{45}$$

3.3 Data structure

The data structure is commonly used to refer to the process of studying the collected data and getting

familiar with its behavior. This process is an effort to enhance the final performance by manipulating

data before feeding it to the algorithm. This process can be started by calculating the correlation value

of inputs among each other and output to detect essential features and check if a similar effect is being

multiplied [55].

The correlation coefficient indicates the dependency between two variables; a high correlation

between input and output indicates the strong dependency of output to the input. However, a high

correlation between two inputs means only one of the inputs needs to be utilized as they are highly

dependent on each other. The correlation coefficient, r_{xy}, between two sets, x and y, can be formulated

as:

$$r_{xy} = \frac{n\sum x_i y_i - \sum x_i \sum y_i}{\sqrt{n\sum x_i^2 - (\sum x_i)^2}\sqrt{n\sum y_i^2 - (\sum y_i)^2}}$$

where n is the number of samples in each set.

Once the correlation coefficients have been calculated, the scatter plot among inputs and target value

can be formed first to check the distribution of inputs and outputs; second, to visually ensure the

relationship of data features calculated using r. Finally, the histogram of the target value will indicate

the expected range output, and the outlier range as a lower count number in the histogram graph will

represent the range that the algorithm will be less confident about. Once these observations have been made, features can be engineered in a way that enhances the performance of any algorithm.

3.4 Feature engineering

Since algorithms enhance their performance using optimization methods such as gradient descent, conjugate gradient, Levenberg Marquardt, etc., scaling will ensure that none of the inputs get an advantage because of scale difference [56]. It also improves the probability of reaching the global minimum instead of potential global ones. Figure **3-10** [57] indicates the effect of scaling on cost function convergence.
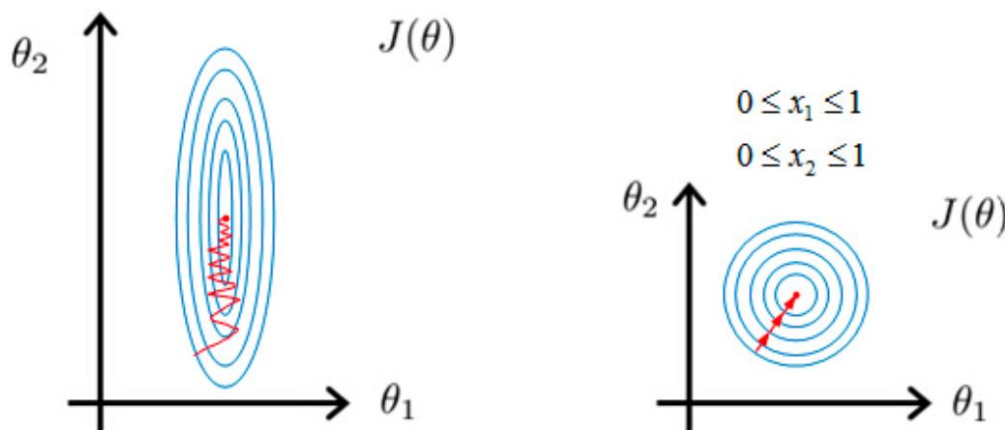
Figure 3-10: Scaling effect [57]

There are different approaches to scale data, such as Z-value, which scales values by their variance after removing the set's mean. Another approach, that has been used in this project, is upper-lower bound scaling, where the input and output values will be scaled between the lower and higher bound[56]. Equation (46) formulates the new value using this method:

$$X_n = ax + b \tag{46}$$

31

$$a = \frac{U - L}{X_{max} - X_{min}}$$

$$b = U - aX_{max}$$

3.5 Data division (Train/Test/Validation)

The processed data now can be used to develop the algorithms and tune the hyperparameters associated with each one. Each algorithm will be developed by utilizing the train/test/validation method. Since all the mentioned approaches are approximation methods for the true function, using the entire data set to develop an algorithm will increase the possibility of over-fitting. Over-fitting happens when the generated solution is highly sensitive to its own inputs and strictly follows the data points instead of the generality of the relation.
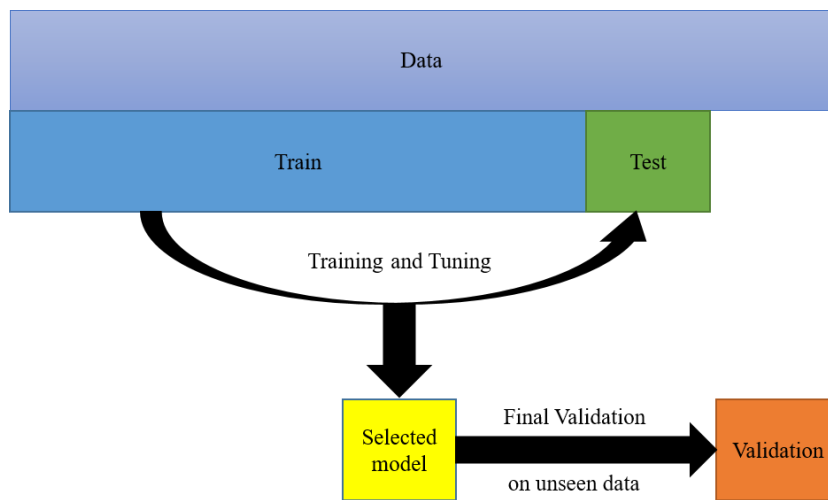
Figure 3-11: Train/Test/Validation process

To avoid this problem, only seventy percent of the data will be used to develop and update the algorithm. The remaining thirty percent will be divided into two different equal sets, test and validation. As indicated in Figure 3-11, the test portion will not be used to tune the parameters, but it will be used to choose the hyper-parameters. Finally, once the algorithm has been trained with the training data, it

will be applied to test data to evaluate the performance of the current setup. In this approach, all the data samples of the training set will be used one by one to update the process, which will result in a slow algorithm. Batching data can be used to overcome this issue.

3.6 Batch processing

Batch processing will split the training set into a specified number of subsets that will be used to train the system at each iteration. Applying this method does not mean that the algorithm would not use the entire training set; it just means that only a batch of data will be utilized through each iteration. This method allows the network to converge to the optimal solution faster than using all the training data each time. As indicated in Figure 3-12, the cost reduction will look like a drunk person walking down the hill, it will not take the best step at a time, but it will descent faster.
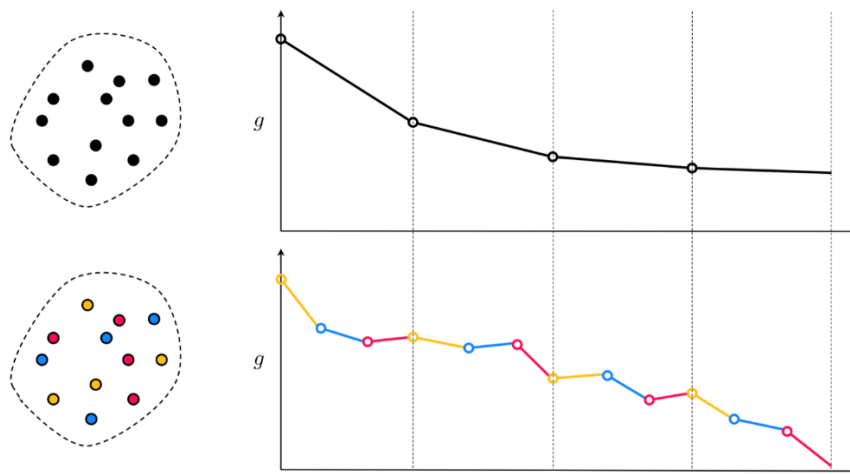
Figure 3-12: Batch processing effect on gradient decent optimizer

Once the models are developed after applying already mentioned techniques, their performance should be effectively evaluated.

3.7 Performance measurement

Once the algorithm is developed based on training data with specific parameters, its performance should be evaluated both on training and testing data sets. Therefore, after completing the training step, a set of predictions using both training and test values will be generated and compared to the actual associated values.

The evaluation is based on Root-Mean-Square-Error (RMSE) and R-Squared (RS, R^2), which is a statistical measure indicating the amount of variation of target explained by inputs $RSME$, and R^2 the calculation is shown in (47) and (48). The best performance setup on both training and testing will be chosen. Finally, the property of the best algorithm will be applied on an unseen validation portion to choose the best algorithm within the three mentioned methods among the best performances within each method. The algorithm that performs properly on all the portions will be chosen as the best algorithm representing the true function. The process is summarized in Figure 3-13.
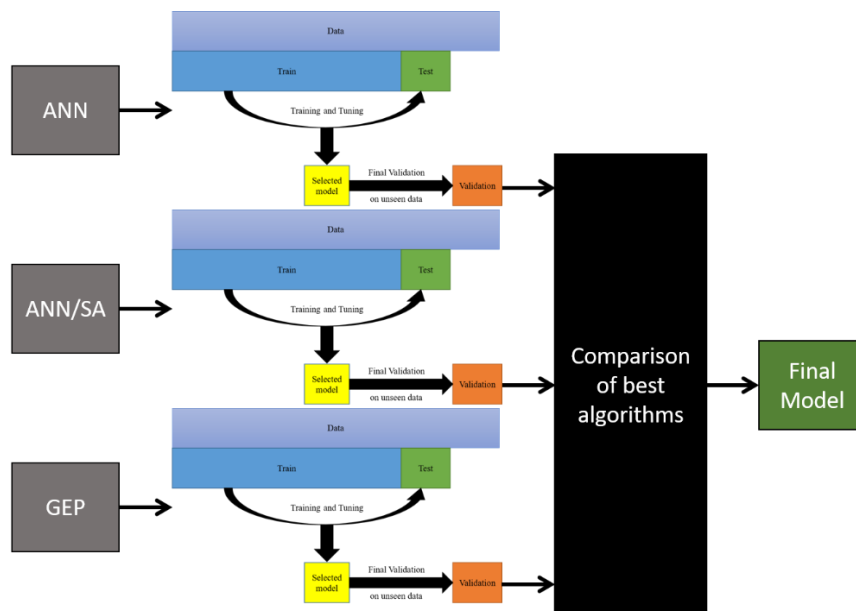
Figure 3-13: Model selection process

34

$$RMSE = \sqrt{\frac{\sum_{i=1}^{N}(y_i - \hat{y}_i)^2}{N}} \tag{47}$$

$$RS = R^2 = 1 - \frac{\sum_{i=1}^{N}(y_i - \hat{y}_i)^2}{\sum_{i=1}^{N}(y_i - \bar{y})^2} \tag{48}$$

Where y_i, $\hat{y}_i$, $\bar{y}$, and N are the actual, predicted, mean of actual set values, and the number of samples, respectively. Though the RMSE and RS of validation data are enough to ensure developers of the performance of an algorithm, other performance parameters can be considered.

3.8 Additional performance measurement parameters

In order to decrease the chance of under-representing the true function, some parameters can be measured. Some of these measurements are simply dealing with errors caused by actual and predicted values, and others check the predictive ability of the algorithm. Mean Absolute Error (MAE) and Mean Absolute Percentage Error (MAPE) in addition to RMSE can be compared among validated models.

$$MAE = \frac{\sum_{i=1}^{N}|y_i - \hat{y}_i|}{N} \tag{49}$$

$$MAPE = \frac{100}{N}\sum_{i=1}^{N}|\frac{y_i - \hat{y}_i}{y_i}| \tag{50}$$

Moreover, one of the slope regression lines through origin k or k' should be closed to 1. Either the squared correlation coefficient between predicted and actual values (Ro^2), or the coefficient between actual and predicted values (Ro'^2) both through origin should be close to 1[58]. Finally, the performance indexes, m and n, should be less than 0.1 [59]. All these values can be calculated using equations:

$$k = \frac{\sum_{i=1}^{N}(y_i \times \hat{y}_i)}{y_i^2} \tag{51}$$

$$k' = \frac{\sum_{i=1}^{N}(y_i \times \hat{y}_i)}{\hat{y}_i^{\,2}} \tag{52}$$

$$m = \frac{R^2 - Ro^2}{R^2} \tag{53}$$

$$n = \frac{R^2 - Ro'^2}{R^2} \tag{54}$$

where,

$$Ro^2 = 1 - \frac{\sum_i^N(\hat{y}_i - y_i^o)^2}{\sum_i^N\left(\hat{y}_i - \overline{\overline{\hat{y}_i}}\right)^2} \tag{55}$$

$$Ro^2 = 1 - \frac{\sum_i^N(y_i - \hat{y}_i^o)^2}{\sum_i^N\left(y_i - \overline{y_i}\right)^2} \tag{56}$$

$$y_i^o = k \times \hat{y}_i \tag{57}$$

$$\hat{y}_i^o = k' \times y_i \tag{58}$$

Chapter 4

System of Coils and frame design

As mentioned before, the magnetic manipulator system developed in this research contains nine coils to achieve 5 DOF manipulation over the working space. In this chapter, the design procedure of a coil with respect to the power consumption, the working space radius, the coil manufacturing process, the core effect, and axial force magnitude are described. Then, coil properties are formulated, and the system configuration is explained. Finally, the frame designed for the configuration used in this research has been presented.

4.1.1 Fabry Factor

Traditionally, Fabry Factor, also known as the Geometry factor or G factor, is used to optimize the dimensions of an air-core coil that produces maximum field at its center while consuming the least amount of power. The G-factor relates the coil's outer radius and height to the inner radius defining a cost function G that needs to be maximized to calculate the optimal values [60]. G factor can be calculated as:

$$G(\alpha, \beta) = \frac{1}{5}\sqrt{\frac{2\pi\beta}{\alpha^2 - 1}} \ln \frac{\alpha + \sqrt{\alpha^2 + \beta^2}}{1 + \sqrt{1 + \beta^2}} \tag{59}$$

$$\alpha = \frac{r_{out}}{r_{in}} \tag{60}$$

$$\beta = \frac{l}{2r_{in}} \tag{61}$$

Where $r_{out}, r_{in}, and\ l$ are the outer radius, inner radius, and length of the coil. The cost function had

been optimized using the fmincon function in MATLAB. Figure 4-1 indicates the surface and contour

plot of the G Factor and its optimal value. Figure 4-1 indicates the optimal values for α, β, and G.
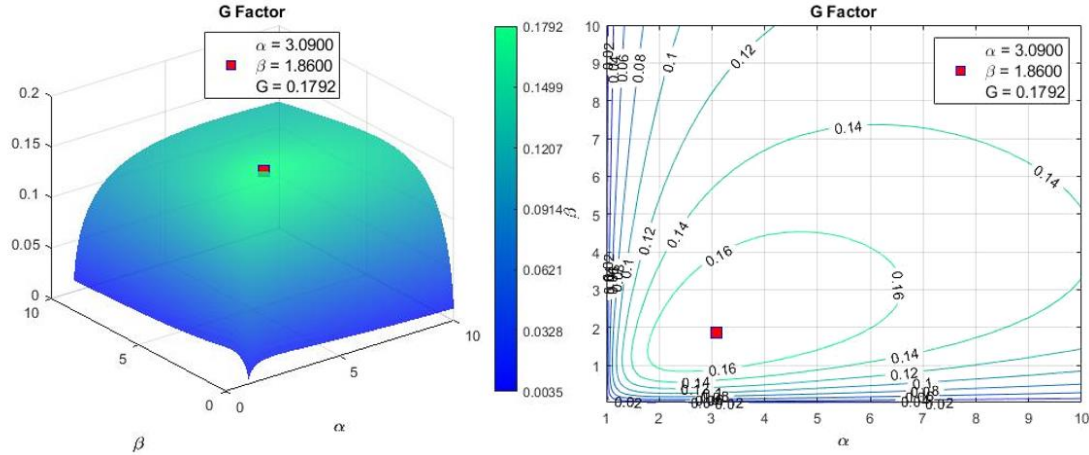
Figure 4-1: Fabry Factor surface and Contour Plot

Since this factor relates coil dimensions with the power consumption, it has been utilized in this

project to select the coil dimensions that produce the most axial force on the coil axis at the furthest

point of the working area. The axial force had been chosen since force manipulation is related to the

field's gradient and more challenging to manipulate than the torque. To use equation (59), the geometric

constraint of the system needs to be defined.

4.1.2 Geometric Constraints of the System

The working space of the coils is a spherical shape, where the center of it is the common intersection

point of the axis of the coils. Since the magnetic field is inversely related to the distance, each coil must

be as close as possible to the sphere's center; meaning, the sphere's radius will directly affect the outer

diameter of each coil.

As indicated in Figure 4-2, the objective is to find the relationship between the sphere radius and the maximum length of each plane just before the intersection points. The length of each plane represents the diameter of the coil. Since each coil will have the same diameter, the lower part of the 2D plot will be evenly divided by three. By implementing a simple geometry, the angles of each triangle will be 60°. Each coil also is a uniform cylindrical, which its center is located at the center of the outer diameter; therefore, $\alpha = 30°$. The relationshop between R_{out} and R_{sphere} is:

$$tan(\alpha) = \frac{R_{out}}{R_{sphere}} \rightarrow R_{out} = 0.57735 \times R_{sphere} \tag{62}$$
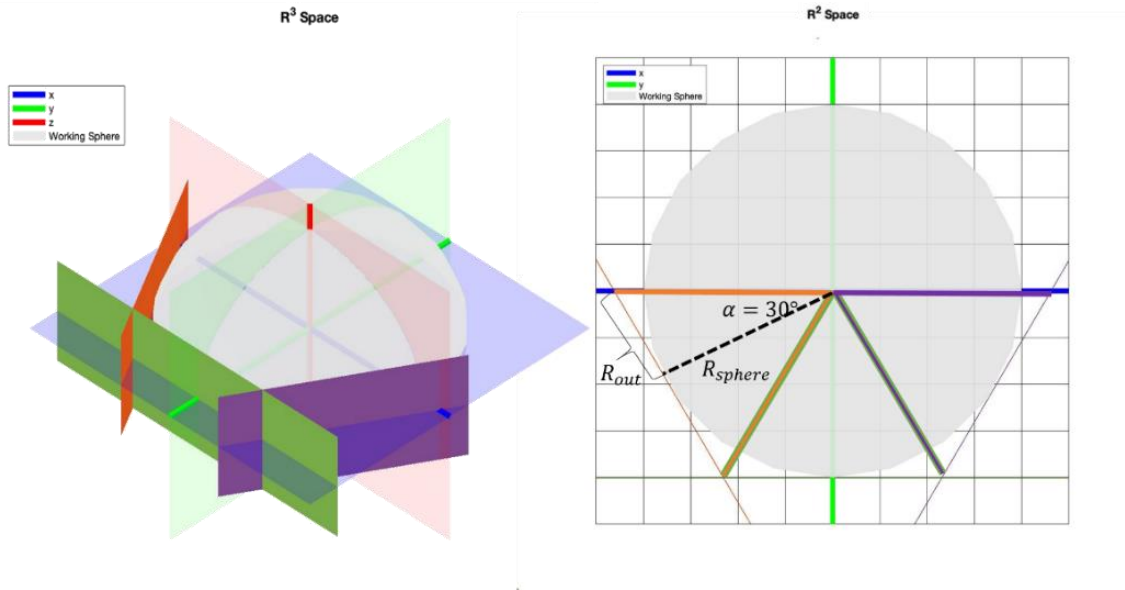
Figure 4-2: The representation of spatial constraint

The spherical radius of 60 mm had been chosen, which makes the largest diameter of each coil equal to $d_{out} \leq 69.2820\ mm$. Since wire diameter, number of layers, number of turns, and the length of the coil are directly related to each other. These parameters are essential in coil modeling and manufacturing; hence, their relationship needs to be formulated.

4.1.3 Manufacturing constraints

Winding a coil is challenging because each coil needs to be as tight as possible to ensure that there is no gap in the final product and is as close as possible to the designed one. Figure 4-3 shows the parameters required for accurate coil modeling. In the presented model, the number of horizontal layers (n_h), also called the number of layers, is shown in red; whereas, the number of vertical layers (n_v), additionally called the number of turns, is in blue. The radius of each circle also is the wire radius.

By incrementing the number of layers, the coil model can be developed:

$$r_{out_1} = r_{in} + 2r_{wire}$$

$$r_{out_2} = r_{in} + (3r_{wire} + \sqrt{3}r_{wire})$$

$$r_{out_3} = r_{in} + (5r_{wire} + \sqrt{3}r_{wire})$$

$$r_{out_{n_v}} = r_{in} + \left[(\llbracket 2n_v - 1)r\rrbracket_{wire} + (n_v - 1)\sqrt{3}r_{wire}\right]$$

$$= r_{in} + r_{wire}\left[(2 + \sqrt{3})n_v - (1 + \sqrt{3})\right]$$

(63)

where, r_{in}, r_{out}, r_{wire} are inner, outer, and wire radius, respectively. to calculate the height of the coil (L_{coil}) the following equation can be utilized :

$$L_{coil} = 2n_h r_{wire}$$

(64)

multiplying each layer by its turns and 2π results in the total length of the required wire.

$$L_{wire} = \pi n_h\{2r_{in} + [2 + (n_v - 1)\sqrt{3}]r_{wire}\}n_v$$

(65)
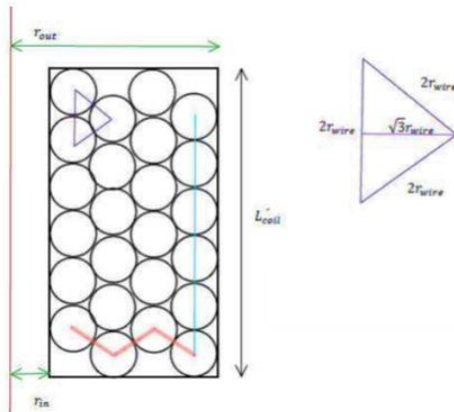
Figure 4-3: Coil design parameters

4.2 Choosing coil dimensions

Since all the required relationships and constraints had been driven, the coil dimensions can be selected. This process initially requires the wire selection and the core placement. The wire type affects the designed coil's resistance and melting point, and the core size and type concern the magnetic field strength and coil's inductance.

4.2.1 Wire selection

Since at least ten amps continues current is considered in this research, AWG14 with the diameter of $1.62814\ mm$ is selected. Considering the coating around the wire, the diameter increases up to $1.73228\ mm$; the area of the wire and its residence are $2.08\ mm$ and $8.286\ \Omega km^{-1}$.

4.2.2 Core

In order to increase the magnetic field's intensity produced by an air-core coil, pure iron with high magnetic permeability had been inserted into the coils [22]. However, they impose a minor change to the system behavior that will be explained later. The core height is equal to the coil height, and its

41

radius is equal to the inner diameter of the coil. In addition to the inserted core, a portable extension part is designed to additionally increase the field strength at the center of the working sphere. According to Figure 4-4, the iron-core coil produces 5.58 more intense filed on average compared to the air-core one.
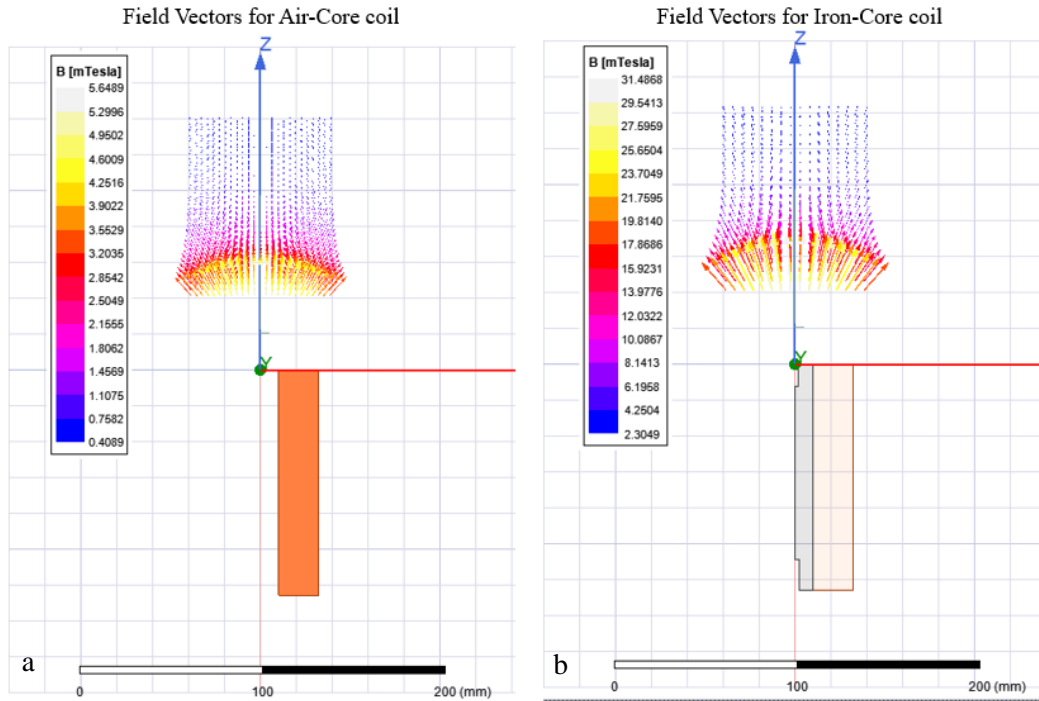
Figure 4-4: Field difference between a) air and b) iron core coil

4.2.3 Inner radius selection

As outer diameter's maximum size had been specified by using (63), an algorithm had been developed, where initially r_{out} was equal to r_{in}. Then, after each iteration r_{in} is decreased by incrementing n_v introduced in Figure 4-3. Using (59), α value has been calculated at each iteration and value to 3.090 has been selected as the feasible optimum value. As shown in Figure 4-5, the optimum feasible α for this system happens at 14 number of layers and is equal to 3.3018.

42
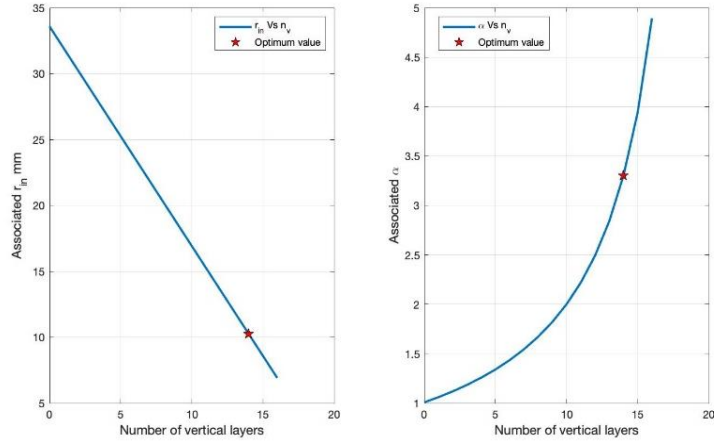
Figure 4-5: The relationship between inner radius, alpha, and number of layers

4.2.4 Length selection

Utilizing equations (59), (60), and (61), various coils were designed and implemented in AnsysMaxwell to calculate the force value at the center of the working sphere over a millimeter cube sphere. Since the outer and inner diameter of the coil is specified, the length of the coil can be calculated subject to the force and G Factor values. Table 4-1 indicates each scenario with associated results.
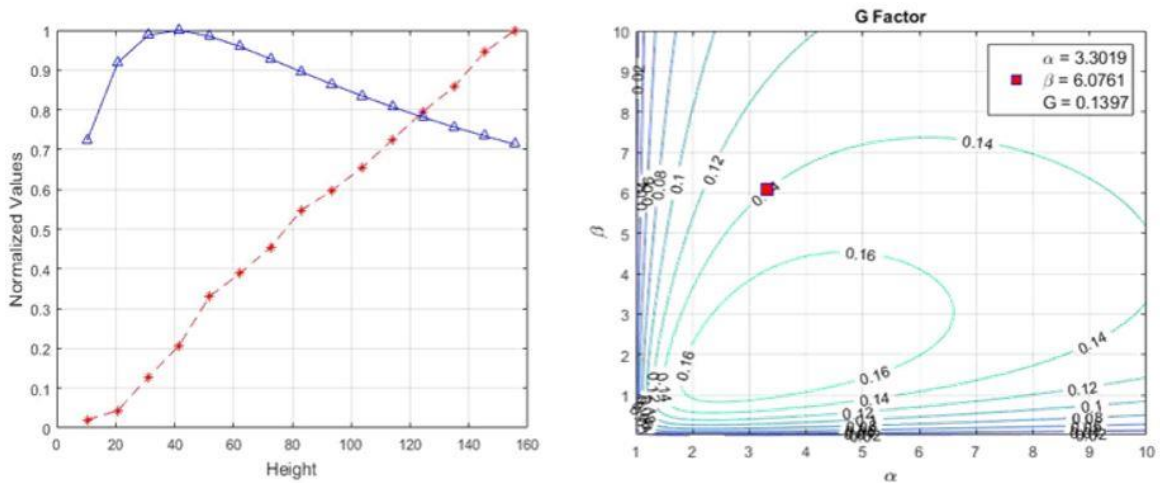
Figure 4-6: a) Normalized G and F values b) Selected coil G Factor

Table 4-1: Variation of Coils with their associated properties and generated force

D_{in} mm	D_{out} mm	n_h	n_v	$N = n_h \times n_v$	Height mm	α	β	G	F mN
20.50	67.69	14.00	6.00	84.00	10.38	3.3019	0.5063	0.129	0.013
20.50	67.69	14.00	12.00	168.00	20.76	3.3019	1.0127	0.164	0.027
20.50	67.69	14.00	18.00	252.00	31.14	3.3019	1.5190	0.177	0.080
20.50	67.69	14.00	24.00	336.00	41.52	3.3019	2.0254	0.179	0.129
20.50	67.69	14.00	30.00	420.00	51.90	3.3019	2.5317	0.176	0.207
20.50	67.69	14.00	36.00	504.00	62.28	3.3019	3.0380	0.172	0.243
20.50	67.69	14.00	42.00	588.00	72.66	3.3019	3.5444	0.166	0.284
20.50	67.69	14.00	48.00	672.00	83.04	3.3019	4.0507	0.160	0.342
20.50	67.69	14.00	54.00	756.00	93.42	3.3019	4.5571	0.155	0.373
20.50	67.69	14.00	60.00	840.00	103.80	3.3019	5.0634	0.149	0.409
20.50	67.69	14.00	66.00	924.00	114.18	3.3019	5.5698	0.144	0.454
20.50	67.69	14.00	72.00	1008.00	124.56	3.3019	6.0761	0.140	0.497
20.50	67.69	14.00	78.00	1092.00	134.94	3.3019	6.5824	0.135	0.536
20.50	67.69	14.00	84.00	1176.00	145.32	3.3019	7.0888	0.131	0.591
20.50	67.69	14.00	90.00	1260.00	155.70	3.3019	7.5951	0.128	0.625

According to Figure 4-6 a, the force value keeps increasing while the length increases; therefore, the G factor is the main parameter choosing the coil with the optimum value. The coil with a 124.56 mm length produces as intense field value as its neighbors but does not waste much power; therefore, it is the optimized one. Figure 4-6 b indicates the α, β, and G values for the selected coil.

4.3 Coil Properties

It is crucial to calculate the properties of the designed coil since they will affect the response time of the coil, its power consumption, and the safety design procedure.

4.3.1 The magnetic permeability of the iron core

Magnetic permeability (μ) is a measurement of the obtained magnetization of a material exposed to a magnetic field, The SI dimension of this property is Henry per meter (H/m).

$$\mu = B/H \tag{66}$$

Where B is magnetic flux density and H is magnetic field strength. Since higher magnetic flux density of a material exposed to the same magnetic field strength is better for the manipulation, a higher value of μ is required. Relative permeability (μ_r) is a dimensionless constant equal to

$$\mu_r = \frac{\mu}{\mu_0} \tag{67}$$

which makes the comparison between materials more convenient.

Pure iron's relative permeability is reported around 4000; Pursuer Company has suggested the annealing chart that increases the irons relative permeability up to 6000 to 8000.
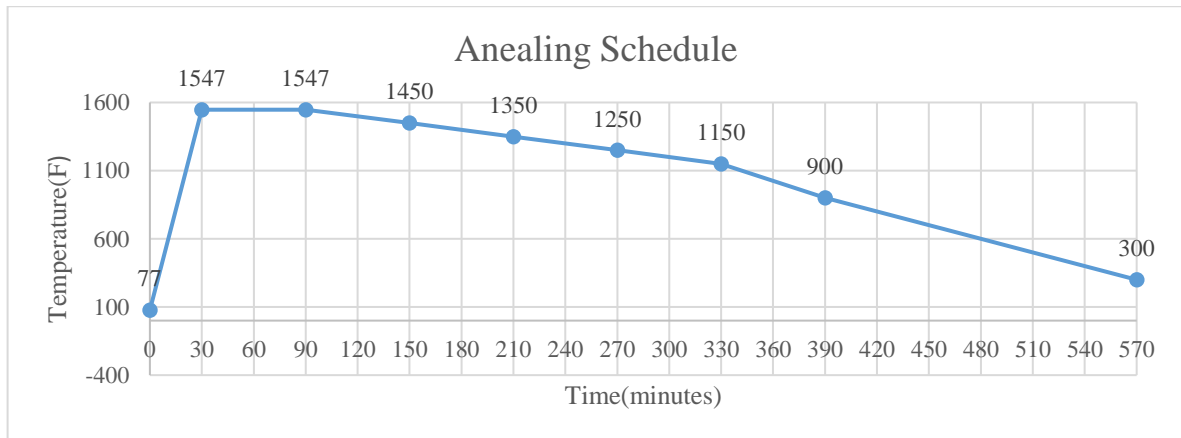
Figure 4-7: Annealing process

45

Figure 4-7 shows the annealing procedure using Argon gas to decrease the possibility of oxidation. Within the first thirty minutes, the furnace temperature boosts drastically to 1547 °F and maintains this temperature for the next sixty minutes. After that, the temperature decreases by an almost steady ratio of 3.65 °F every ten minutes till it reaches 300 °F; after five hundred seventy minutes, the furnace needs to be turned off until iron parts gradually reach room temperature.

4.3.2 Power consumption of a single coil

To calculate the required power of the system, the power consumption of each coil (P) calculated in Watts should be derived:

$$P = RI^2$$
<div align="right">(68)</div>

Where I, measured in amps, is the amount of current and R is the coil's resistance in ohms (Ω). The resistance of the designed coil is equal to:

$$R = \frac{\rho L_{wire}}{A_{wire}}$$
<div align="right">(69)</div>

where ρ is the resistance density, L_{wire} is the total length of wire, and A_{wire} is the wire cross-section area. By applying (65), (69), and the AW14 properties, the resistance of the chosen coil is equal to 1.053Ω. By substituting R into (68) with an anticipated 10 amps current, the required power of each coil is 105.30 Watts.

4.3.3 Coil Inductance

Inductance is another essential property of the coil that directly affects the response time and safety of the system. Inductance is the tendency of a coil to resist the change of the current passing through it. The flowing current produces a magnetic field around the coil. Any variation in the current passing

through the wire will also cause a change in the field's strength; consequently, based on Faraday law, the field's strength changes induce an electromotive change known as EMF voltage [61].

Inductance, symbolled by L with a unit of Henry (H), is the reluctance of a coil to the change of current; the higher the inductance, the slower the coil reaches its desired current. Moreover, higher inductance produces more EMF voltage which can cause damage to other electrical circuit parts in the system. Figure 4-8 shows that Ansys Maxwell reports the value of 75.375 mH for the inductance of the selected coil.

Inductance also affects the stored power inside the coil and can be calculated by (70) where P is power, L is inductance, I is current, and t is time.

$$P = LI\frac{dI}{dt} \tag{70}$$

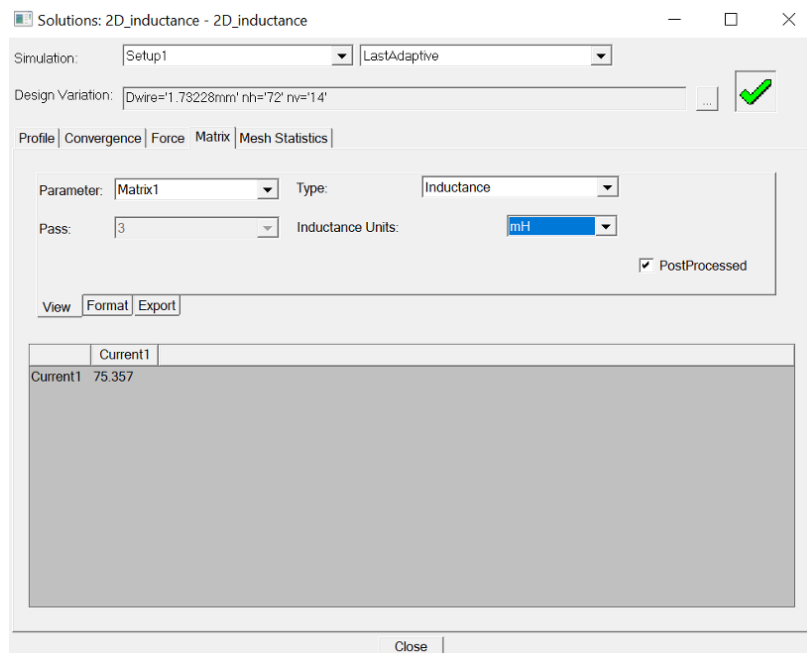By considering the unit rate of change, each coil requires 0.78 Watt.

Figure 4-8: Inductance measurement of the coil

47

4.4 Coils configuration

Several configurations are suggested for magnetic manipulation to reach controllability over the workspace. Since eight coils are required, the Square Antiprism configuration has suggested an atomic shape. In this configuration, each coil is distanced enough from the others to ensure that coils are dependently and linearly affecting the field and close enough to the working space to produce a strong magnetic field. This system arranged each coil normally to a working sphere facing a common point at the sphere's center; coils are evenly spaced, meaning each coil is 60° rotated from the sphere's center. Finally, a group of 4 coils located next to each other is rotated 45° around the sphere's axis.

Octomg has also used the same idea, A set of four coils placed at the lower part of the sphere are deviated from the sphere's axis by 45° individually, then rotated around it 45° as a set. Each coil is initially placed at 90° away from the central axis for the upper side of the sphere. However, later, they deviated 80° from the central axis to enhance the force manipulation.

The Open-Asymmetric configuration inspires the proposed design in this project[62]. The upper sphere deviates 60° from the central axis of the working sphere and includes five coils, then rotates 45° around the sphere's axis. On the other side of the sphere, each coil is 80° deviated from the axis. Figure 4-9 illustrates the configuration; moreover, the Euler angles associated with each coil are summarized in Table 4-2.

The surrounding activated coils will energize the iron core inside a coil with no current passing through it. This phenomenon violates the linear independence of the coils; however, since the permeability of the used core is high, the core is assumed to demagnetize fast enough so that this effect can be neglected.

48
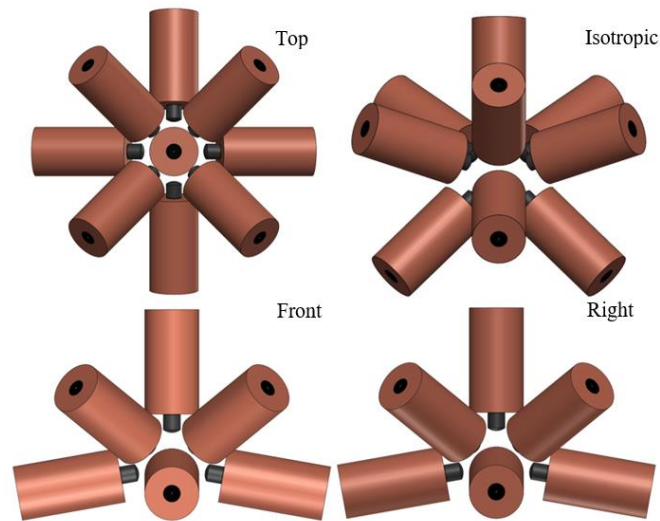
Figure 4-9: Top, front, right, and isotropic views of the configuration

4.5 Frame design

Aluminum extrusion had been used to place the coils in the desired orientations and distances. As indicated in Figure 4-10 a, all the coils are fixed inside a rectangular box, where the box is located on four legs, shown in Figure 4-10 b. This design enables users to have two options studying this system as the box can be rotated and replaced on the legs.
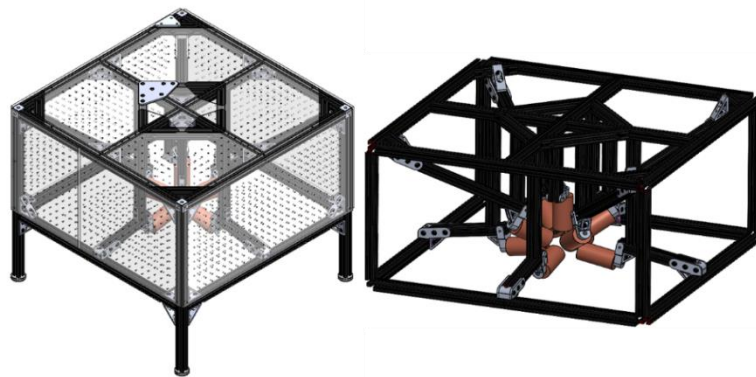
Figure 4-10: a) Entire Frame b) Main body of the design

Moreover, Figure 4-11 indicates that each coil is located on the rail using a pin-hole system that allows accurate coil placement. These holes also provide the advantage of expanding working space and using wider coils using the same frame. Moreover, aluminum extrusions are placed at fixed angles because designing a moveable holder for coils would have made accurate positioning of them a challenging process. Furthermore, this design makes safety-related implementations simple as the rectangular box can be enclosed by transparent sheets like acrylic.
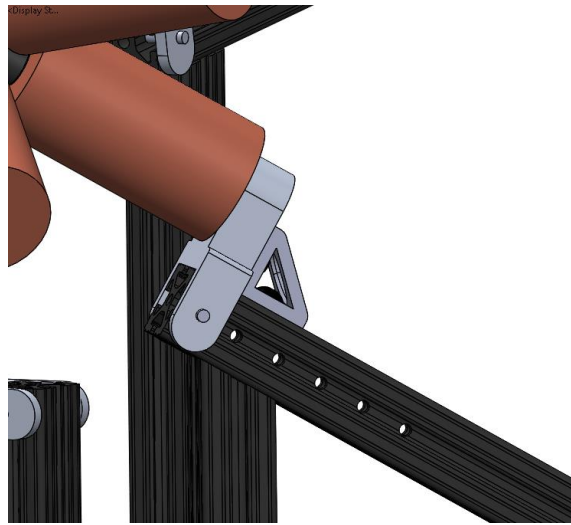
Figure 4-11: Coil holder

Table 4-2: Euler YZY angles

1	2	3	4	5	6	7	8	9
0	-90	-90	90	90	-100	90	100	90
0	45	-45	-45	45	0	-90	0	90
0	30	30	-30	-30	0	10	0	10

Chapter 5

Electrical Design

This chapter discussed the power source selection challenges and describes the electrical equipment selection process. Ultimately, it describes the safety concerns.

5.1 Power source

As calculated before, each coil will consume a maximum of 105.30 Watts; therefore, a system of nine coils' consumed power seems to be around 950 Watts. The power is also required to be supplied in a high voltage to assure that the inductance of the coils will not drastically affect the system's time response. Figure 5-1 indicates that the power supply selection involves the coil power requirement, the inductance concern, and the wall outlet properties. The laboratory this system is installed has a DC 208V single phase outlet; hence, the power supply should be compatible with it.

$$I = \frac{P}{V}$$

Power Supply (P) → Electrical Components → $I_{9 \times 1}$ → System of Coils
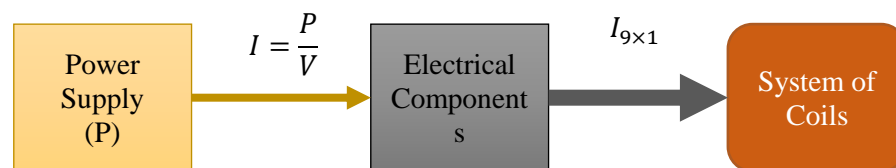
Figure 5-1: Outlet to wall power schematic diagram

Assuming 105 Watts for each coil means that all the coils are receiving the 10 amps maximum current, multiplying by nine coils, the power supply should be able to produce 90 amps current in a high voltage; however, due to the symmetry of eight coils in the designed configuration and assuming the ability to apply negative current, required current can be reduced to 50 amps. Moreover, not all the coils will be operating at their maximum capacity all the time. Therefore, producing only 60% of the maximum current operation, which is equal to 30 amp, should be sufficient for the manipulation.

The amount of required power will be determined by the operating voltage of the electrical components; hence, the gray box in Figure **5-1** needs to be explored. As explained in the the next section, the investigation will result in a maximum of 175 VDC operational voltage; therefore, a 5000 Watts DC power supply is required.

5.2 Servo driver selection

In order to select a servo driver that reads the control unit command and sends the required current to the coils, some essential criteria need to be addressed. As illustrated in Figure 5-2, the servo driver connection type should be compatible with the control unit and the power supply. Moreover, it needs to be able to work on the current model since the coil impedance changes through the experiment; therefore, the servo driver should be able to adjust the current accordingly. Finally, it needs to be able to supply the required current.
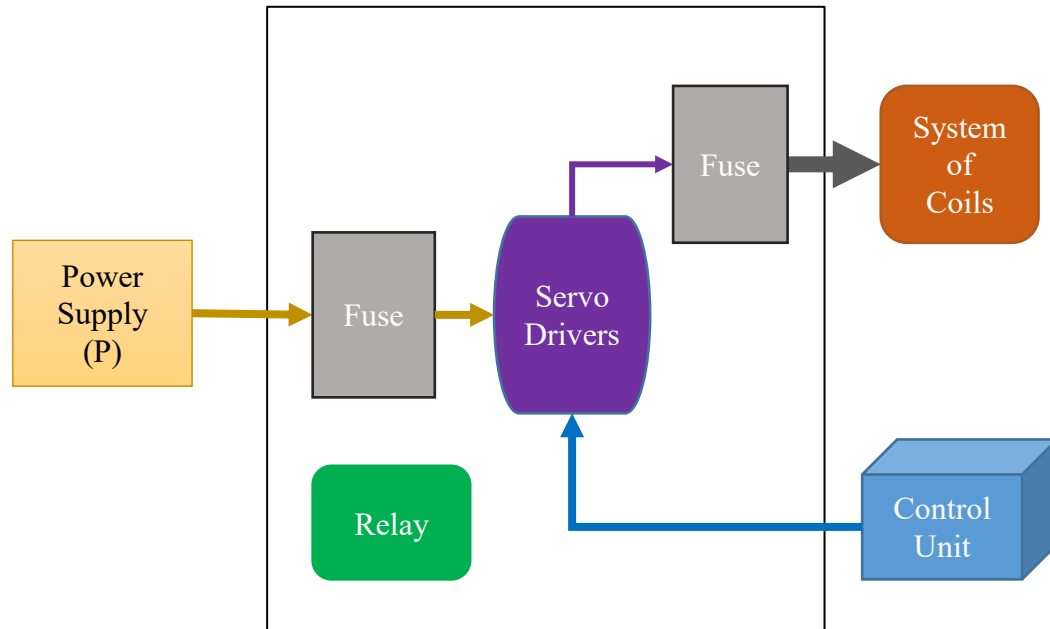
Figure 5-2: Some of the electrical components

According to Table 5-1 the servo driver's supply voltage varies from 40 to 175 voltage in DC mode, meaning that it can handle high DC voltage. Its continuous current carrying capacity is 25 amp, which allows a higher current resolution setup by running it in the half capacity mode. Also, it is sufficient for the desired value of ten amps.

Table 5-1: Servo Deriver's specifications

Current continuous (A)	25
DC supply voltage (VDC)	40-175
Operation mode	Current, duty cycle, velocity, hall velocity tachometer velocity

5.3 Controller

Servo drivers can read the signal sent by the controller and regulate the current at each coil accordingly. Since there are nine coils and servo drives, the controller needs to have at least nine output channels; it also requires operating at the same voltage range as derivers, at ± 10 V.

5.4 Safety concern design

The supplied power into the system is more than 100 watts, so safety matters should be considered in the electrical design of the system. **Error! Reference source not found.** b indicates that the power supply is restricted in an aluminum box to ensure that wires are not exposed during the experiment. Moreover, the ground wire shown in green, coming from the wall outlet, is connected to the power supply output and the designed box; hence, the entire system is connected to the same ground.

Generated power goes through a relay connected to the coil frame using a limit switch. If the switch is closed, meaning that the door is locked, the power will be distributed in the system. However, once the door remains open or suddenly opens during the experiment, the drivers will not get any power, and

the system will shut down. The servo drivers, the relay, and the power distributors are enclosed using another box, which is also connected to the same ground wire as previous parts. To avoid accessing exposed wires, each coil and associated servo driver are connected through an industrial connector. Red wire indicates the positive current, black represents the negative charge, and purple is the signal wire coming from the control unit.

Furthermore, the fuse boxes cut the circuit if the current goes above the desired value to ensure that none of the equipment gets damaged. After the power supply output, a diode was also implemented to warranty that the back emf voltage does not cause any problem in the system as the current direction does not change.
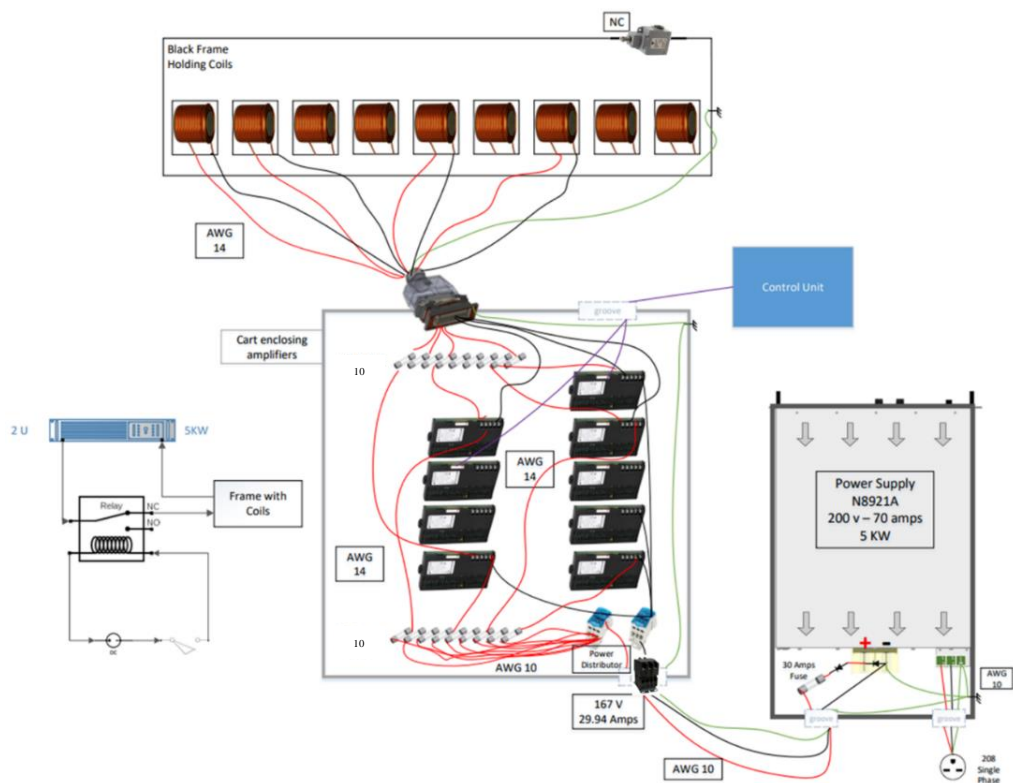
Figure 5-3: The electrical design of the system

The frame is enclosed using acrylic sheets with holes of 4mm diameter large on them. This sheet has a melting point of 82 °C which is more than the experiment temperature. According to Figure 5-4, at a maximum of 10 amps, the coil will reach 31.27 °C starting from the room temperature working continuously for 60 seconds. The ratio of the change with maximum current is almost 6 °Cmin^{-1}, so it takes ten minutes to reach the melting point of the sheet, which is considerably higher than the experiment timeframe.
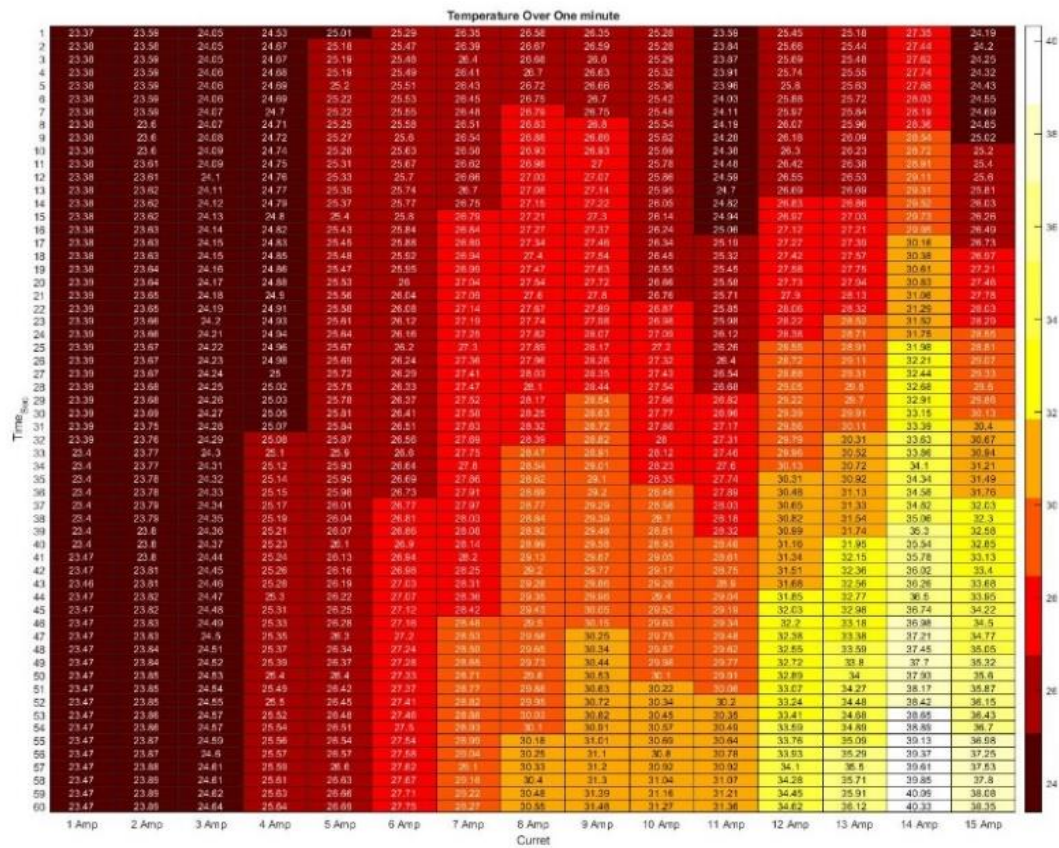
Figure 5-4: Coil temperature for time versus current

Chapter 6

Experiments

This chapter explains all the experimental works, including the modeling validation of the coil, conducting different approaches to measure its property, followed by developing the dataset required for the regression models. Moreover, it discusses the results of the regression models and presents the optimum technique. Finally, the control logic of the manipulation will be developed.

6.1 Designed coil

Validation of the coil modeling starts by measuring its dimensions, resistance, and inductance. As Figure 6-1 indicates, the fabricated coil's length and diameter are equal to $124.5mm$ and $66.64mm$, respectively. Table 6-1 indicates the designed and actual dimensions of the coil accompanied by the associated errors. Equations (63), (64), and (65) have modeled the coil dimensions with less than three percent error; further, the resistance is modeled with only four percent error.

Figure 6-1: Manufactured coil

Table 6-1: Properties of the coil

	Designed coil	Manufactured coil	Error%
Outer radius	$67.69 \ mm$	$66.03 \ mm$	2.5140
Length	$124.56 \ mm$	$124.28 \ mm$	0.2253
Resistance	$1.053 \ \Omega$	$1.1 \ \Omega$	- 4.2727

6.2 Inductance

Once the coil's resistance is known, the inductance can be measured. Three different methods have been implemented to ensure that the small capacity created by any coil will not affect measuring the actual inductance value. Then, the results of these three methods are averaged and considered the final value.

6.2.1 Cut-off frequency

Since at the cut-off frequency, presented as f in Hertz, the impedance and voltage of the R and L components across the circuit are the same, L can be developed as:

$$@ \ V_L = V_R \ \rightarrow \ Z_L = Z_r \tag{71}$$

$$2\pi f L = R \tag{72}$$

$$L = \frac{R}{2\pi f} \tag{73}$$

Figure 6-2 a indicates the RL circuit used in this experiment; a resistor of 43.4Ω had been added to the system. The summation of this resistor and the coil's resistance is equal to the circuit's total resistance. At the frequency of $93.15 \ H$, the voltage across both components was equal to $1.378 \ v$ shown in Figure 6-2 b.
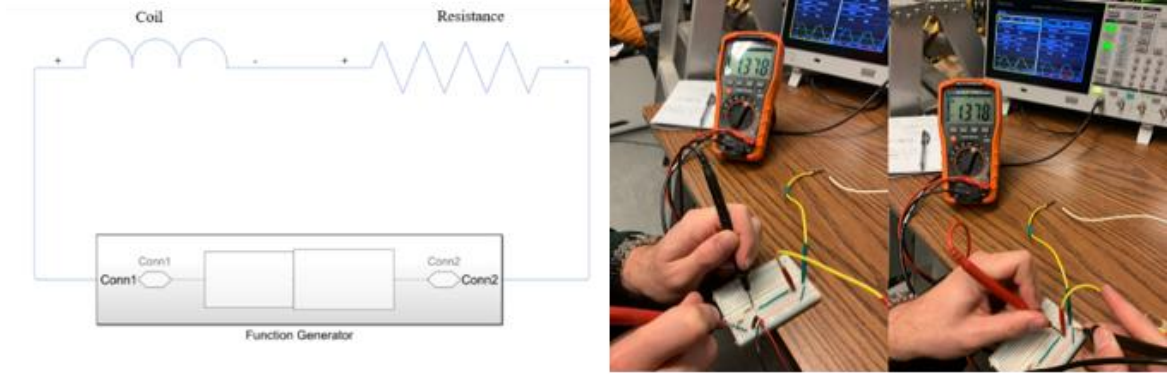
Figure 6-2: a) RL circuit of the cut-off frequency b) Voltage across R and L

Therefore, by implementing the values into (73):

$$L = \frac{43.4 + 1.1}{2\pi \times 93.15} = 74.2 \, mH \tag{74}$$

6.2.2 Phase difference RL circuit

In order to ensure that the system is not sensitive only to the added resistance and producing results based on constant capacitance, the resistance on the circuit is changed to 21.8 Ω. As Figure 6-3 a indicates, the function generator has a 50 Ω resistance built-in; since the oscilloscope could not eliminate the effect of the built-in resistance, it will be added to the total resistance. The phase difference between source and resistance, symbolized as ϕ, could result in formulating L as:

$$Z_L = j\omega L \tag{75}$$

$$Z_R = R \tag{76}$$

$$f_{cut-off} \rightarrow |Z_L| = |Z_R| \tag{77}$$

$$L = \frac{R}{\omega} = \frac{R}{2\pi f} \tag{78}$$

$$\frac{V_R}{V_{source}} = \frac{R}{j\omega L + R} = \frac{R}{jR + R} = \frac{1}{1 + j} \tag{79}$$

$$\phi = 45° \tag{80}$$

Figure 6-3 b indicates the oscilloscope's output where the required phase difference satisfies (80); hence,

$$L = \frac{50 + 1.1 + 21.8}{2\pi \times 163} = 71.2 \; mH \tag{81}$$
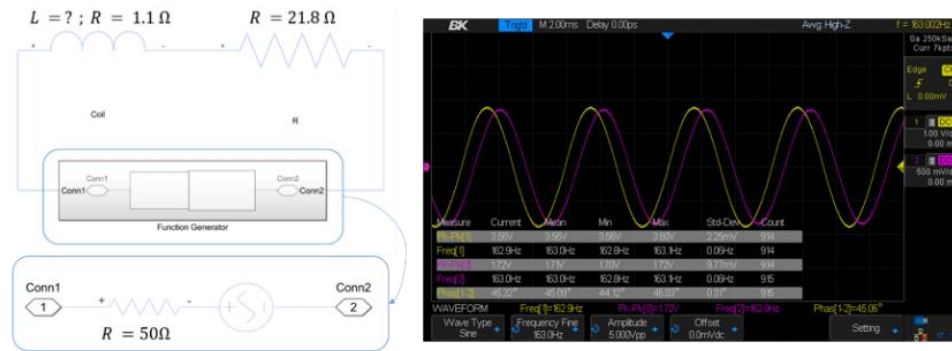
Figure 6-3: a) RL circuit for phase difference b) Oscilloscope output

6.2.3 Step response approach

The last approach is based on the step response of the current passing through the coil. Since the steady-state response of the coil to reach the desired output, shown in Figure 6-4, is affected by the inductance and resistance of the coil, forming the current equation in the time domain and collecting the current values from an oscilloscope will result in L calculation.
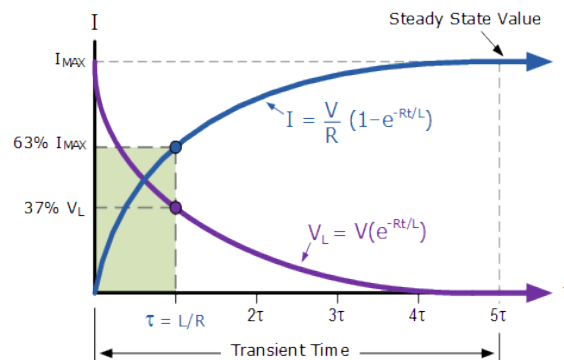
Figure 6-4: Steady-State response

59

$$V_{(t)} - V_R - V_L = 0 \qquad (KVL\ approach) \tag{82}$$

$$V_R = I \times R \tag{83}$$

$$V_L = L \times \frac{di}{dt} \tag{84}$$

$$V_{(t)} = I \times R + L \times \dot{I} \tag{85}$$

$$I_{(t)} = \frac{V_t}{R}\left(1 - e^{-\frac{Rt}{L}}\right) \tag{86}$$

$$I_{(t)} = \frac{V}{R}\left(1 - e^{-\frac{t}{\tau}}\right) \tag{87}$$

$$\tau = \frac{L}{R} \tag{88}$$

As shown in Figure 6-4, 5τ is were system gets to the steady-state value. Figure 6-5 is the illustration of collected data for the manufactured coil. Since current reaches its steady-states value after $\Delta t = 6.598$ milliseconds:

$$L = \frac{\Delta t R}{5} = 66.51\ mH \tag{89}$$
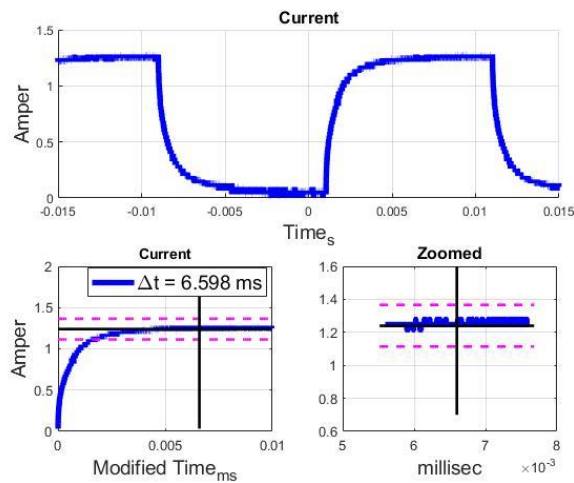
Figure 6-5: Step response of the current

60

Table 6-2 includes the measured and the simulated inductance values mentioned at (74), (81), (89), and Figure 4-8; the average inductance is equal to 70.64 mH, which is only 4.72 percent less than the simulated value.

Table 6-2: Inductance measurements

Approach	Value in mH	Average mH	Error mH
Cut-off frequency	74.2		
Phase difference	71.2	70.64	
Step response	66.51		4.72
Ansys Maxwell	75.36	75.36	

The response time of the coils leads to tuning the servo drives on their fastest response mode. Figure 6-6 indicates the tuning response of one of the coils, where the required time reaching the steady-state value is equal to 6.76 ms.
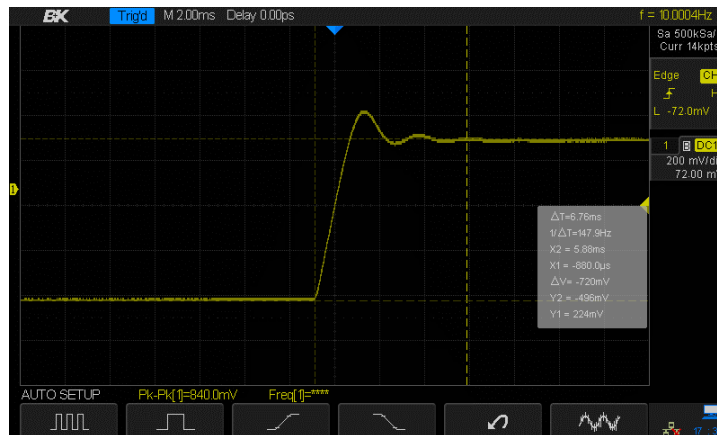
Figure 6-6: Servo driver tuning

6.3 Superposition

Figure 6-7 indicates validating the superposition assumption. As indicated in Figure 6-7 a and Figure 6-7 b, two coils are placed 124 mm away, and a gauss meter probe is positioned at the middle of them.
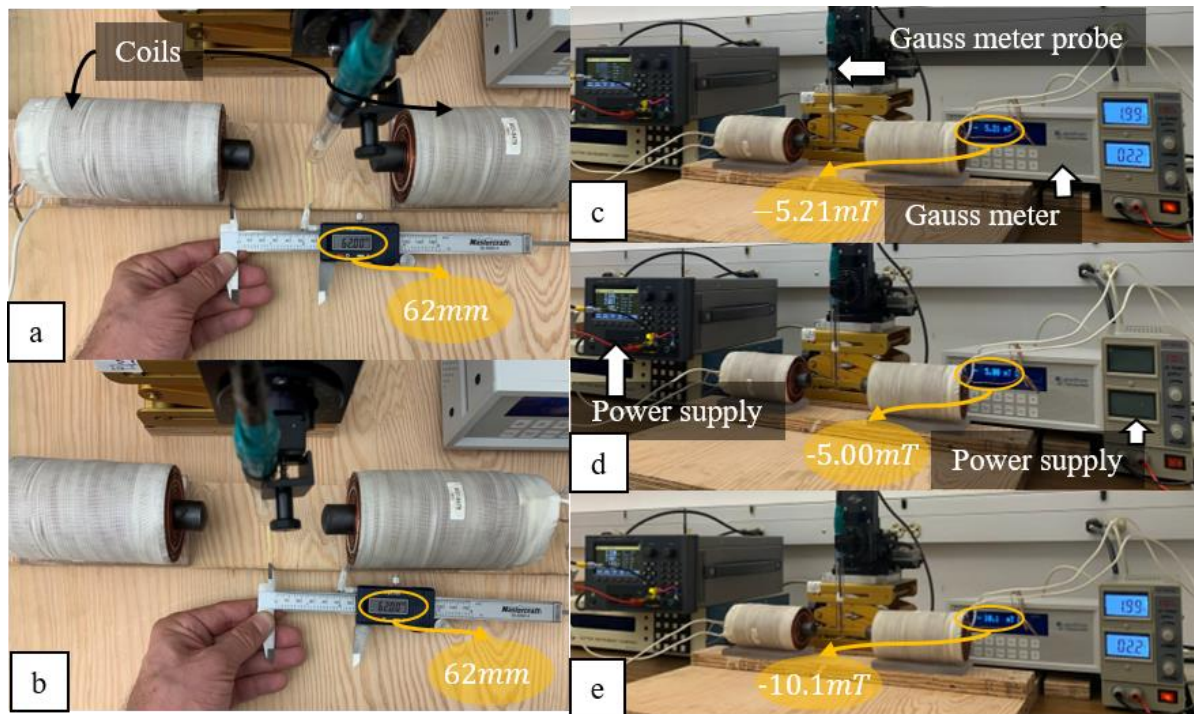
Figure 6-7: Superposition validation a) left coil placement b) right coil placement c) right coil activation d) left coil activation e) simultaneous activation

Figure 6-7 c shows that when the left power supply is off, a 2 amp current through the right coil causes a magnetic field of -5.21 mT. Similarly, Figure 6-7 d demonstrates that the left coil will generate -5.00 mT. Ultimately, Figure 6-7 e shows -10.1 mT for both coils being activated, which is only 1.09 percent less than the summation of each coil's individual contribution; therefore, the magnetization of the cores can be neglected.

6.4 Magnetic permeability

In order to confirm the permeability of the core magnetic field value of several points on the axis of the coil had been measured using a gauss meter and compared to FEM results. The design indicated in Figure 6-8 has been developed in the 2D environment using very fine mesh sizes. The 2D environment takes advantage of the symmetry of the coil and decreases the number of nodes considerably compared to the 3D environment, and produces more accurate results than the 3D one. The mesh properties are shown in Table 6-3. As indicated in Figure 6-8 b, the simulation was stopped when the error value was less than 0.0002 to ensure the simulation's accuracy.
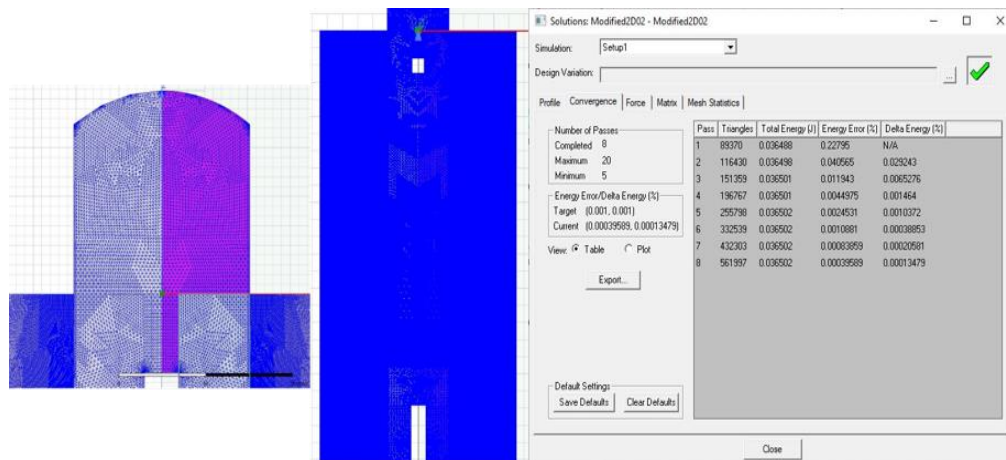
Figure 6-8: a) Mesh size illustration b) Simulation termination

As indicated in Figure 6-9, the model developed for the air-core coil at (11) perfectly matches the simulation values; hence, the 2D design with the proposed coil and background mesh size is a reliable source for the proof check. It also indicates that the experimental data matches with the simulations developed for an iron-core coil with the $\mu_r = 8 \times 10^3$. This observation confirms that the annealing process had been done correctly.

Table 6-3: Mesh properties

	Number of Elements	Min edge length	Max edge length	RMS edge length	Min element area	Max element area	Mean element area	Std Devn (area)
background	89861	1.68E-08	5.51E-03	8.23E-04	3.27E-16	8.27E-06	2.87E-07	5.09E-07
Coil	404742	1.96E-05	4.25E-04	1.27E-04	2.21701e-10	5.08E-08	6.91E-09	4.67E-09
Core	28473	1.15E-05	4.99E-04	3.16E-04	8.70371e-11	1.02E-07	4.29E-08	1.85E-08
Extension _Core	4886	3.92E-08	5.00E-04	3.21E-04	2.97E-15	1.01E-07	4.45E-08	1.74E-08
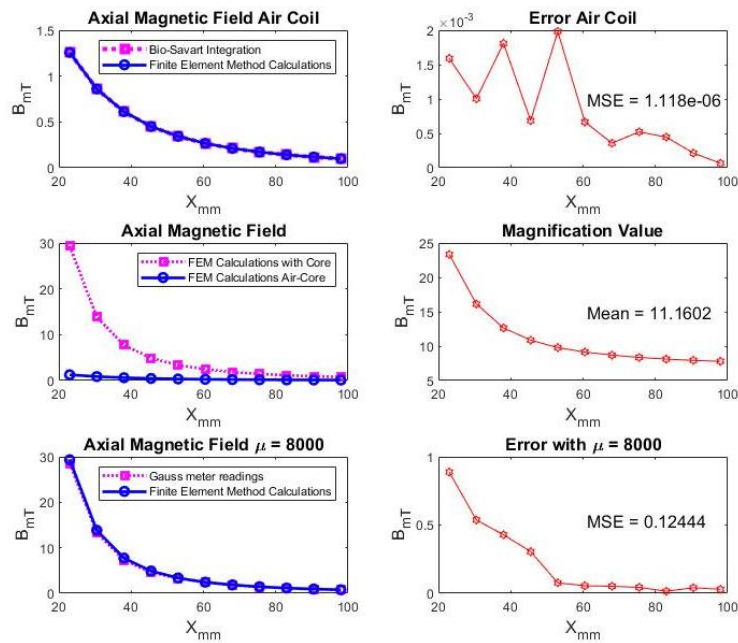
Figure 6-9: Modelling validation

However, the 3D simulation has not matched the experimental results; as shown in Figure 6-10, the simulated value on average is 16.81 less than the actual one. Increasing the accuracy of the 3D simulation would have been computationally expensive; therefore, a dataset had been developed to benefit from artificial intelligence algorithms for magnetic field prediction.
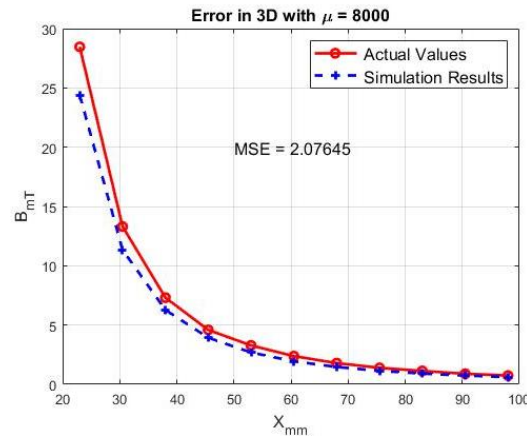
Figure 6-10: FEM and actual magnetic field values

6.5 Artificial intelligence algorithms development

In this research, supervised learning had been used where each set of input is associated with an output value called target; the input value is the position of the desired point in the working space, $\vec{P}$, and the target value is the magnetic field, $\vec{B}$. For each component of the magnetic field vector, a separate algorithm was developed to ensure the accuracy of the prediction.

6.5.1 Data collection

Magnetic field values had been collected using a gauss meter probe attached to a micromanipulator with a range of $25mm$ at each direction. A cubic region of $20 \times 22 \times 22$ coincide at the center of the working space sphere with a spacing of $2mm$ had been chosen for data collection. Figure 6-11 indicates

the system used to collect 1728 samples for each magnetic field component, meaning that 5184 samples had been collected in total.
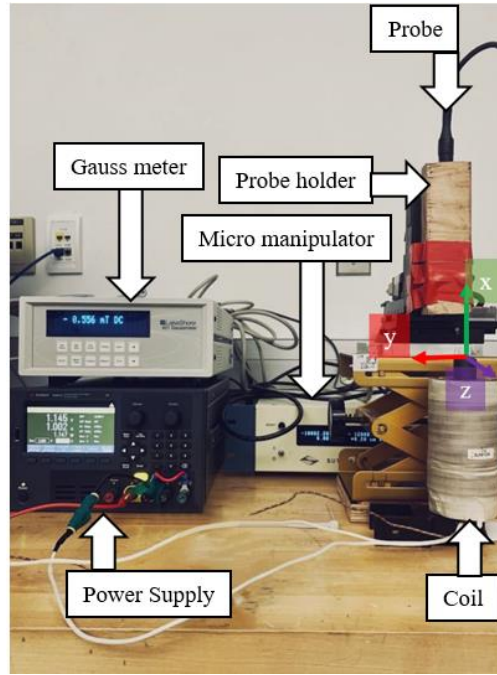
Figure 6-11: Collecting data for a unit current

6.5.2 Data structure

After successfully collecting the data, it is essential to understand the relationship between each input and the required target. As indicated in Figure 6-12, the same position component as the field component is highly related to the field value, whereas the other two components do not form a linear association. As verified in Figure 6-12 b, the diagonal plots illustrate an almost linear relationship with the associated target values. Furthermore, as the P_x value grows, B_x value converges toward zero; however, an increase in the P_y and the P_z absolute values result in stronger B_y and B_z. Figure 6-12 c also reveals that B_x has the highest mean value and varies almost twice as many other field components.
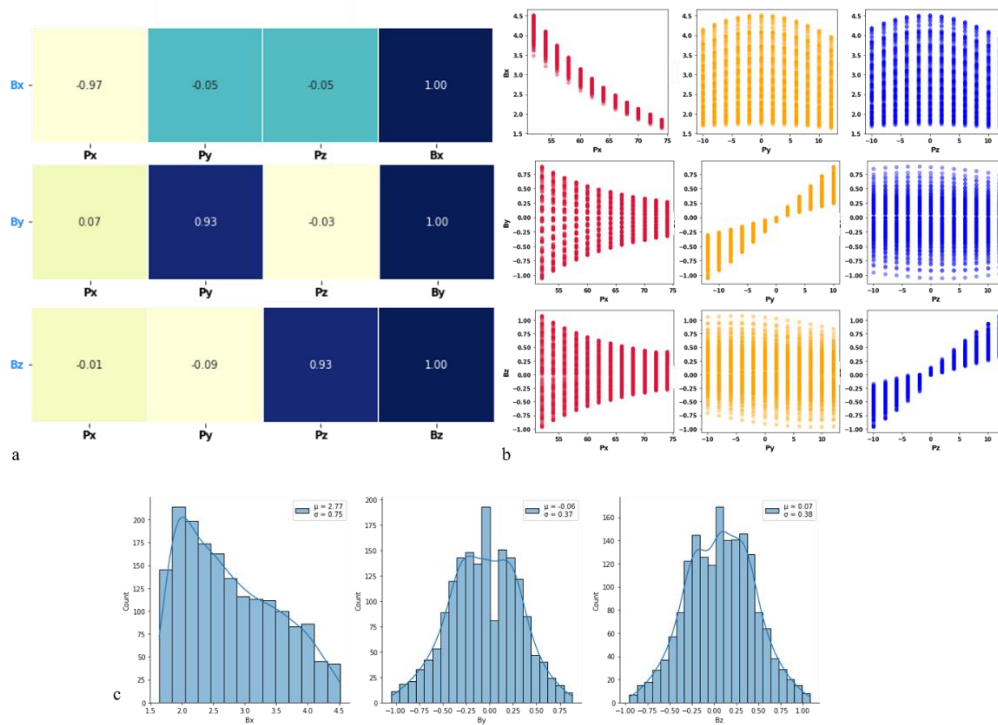
Figure 6-12: a) Correlation of each input and target values. b) Scatter plot of inputs and target

values. c) Histogram of each target

Figure 6-12 shows that the general expectations for the field shape are met, and data is appropriately

collected; therefore, regression algorithms can be implemented.

6.5.3 Algorithm Development

Each target has its algorithm separately developed for each method. However, to ensure that the

algorithms receive the same samples, the data set associated with B_x, B_z, and B_z had been randomly

shuffled and split following the explained train/test/validation method. The training data is consists of

1216 samples, and both test and validation sets contain 256 samples. The first developed algorithm is

ANN.

6.5.3.1 Artificial neural network (ANN)

The network had been developed using the TensorFlow library in the Google Colab environment. This library enables users to define each layer individually and specify properties like random initial weigh generator, activation matrix, and the number of neurons at each layer. It also lets users choose the loss function type and learning rate. For this project, the adam optimizer, stochastic gradient descent method, learning rate of 0.001, and batch size of 64 had been chosen.

Only one hidden layer with four to seven neurons activated with the relu function had been examined. Since this is a regression problem, the linear combination of the neurons and bias will form the output. As shown in Figure 6-13, the output of the relu function is equal to zero for inputs less than zero, and it is equal to the input for those more than or equal to zero.
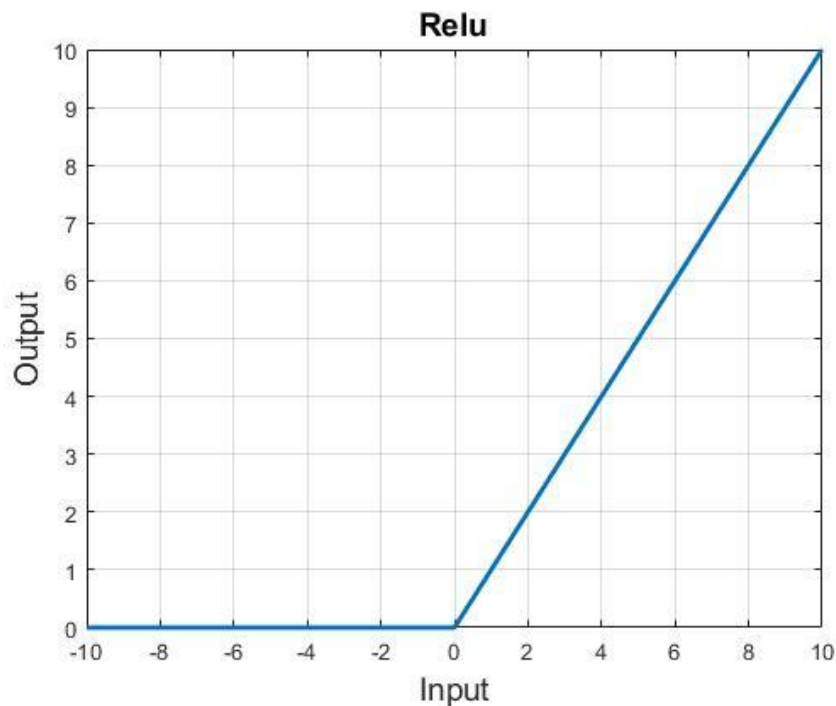
Figure 6-13: Relu Function

In order to choose the optimum number of neurons in the hidden layer, the Root Mean Square Error $RMSE$ and the coefficient of determination R^2 of each output had been plotted for both train and test sets as the decision-making parameter; the highest R^2, and lowest $RMSE$ represents the optimum scenario.

As Figure 6-14 indicates, the second scenario, associated with five neurons, yields optimum weight adjustment for B_x. On both Train and Test sets, it has the highest R^2 and lowest $RMSE$ values. Moreover, the R^2 values are more than 0.8; therefore, there is no need to add another layer.
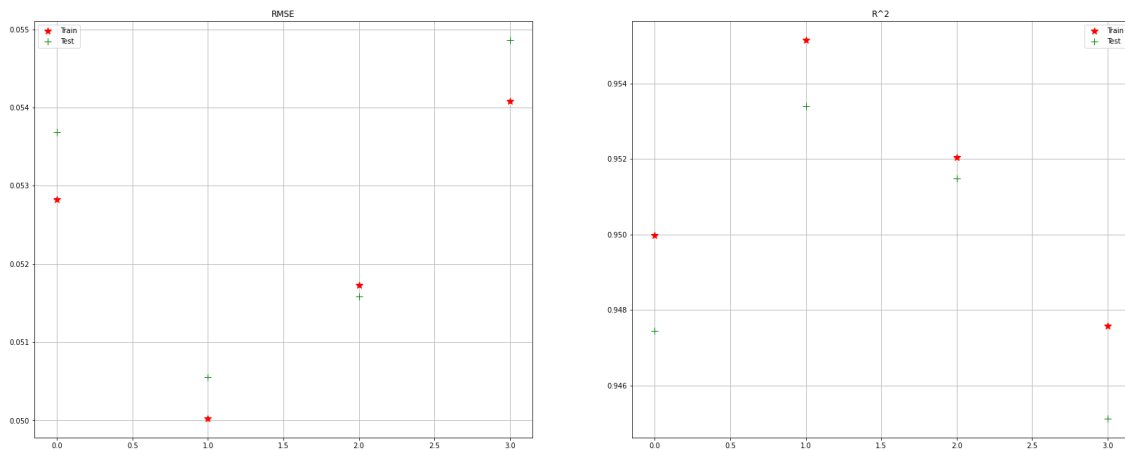
Figure 6-14: ANN network for B_x a) $RSME$ b) R^2

According to Figure 6-15, five hidden neurons provide R^2 more than 0.950 on all the datasets with almost similar $RMSE$ values. However, considering the output range of 0.05 to 0.95, the error value seems high.
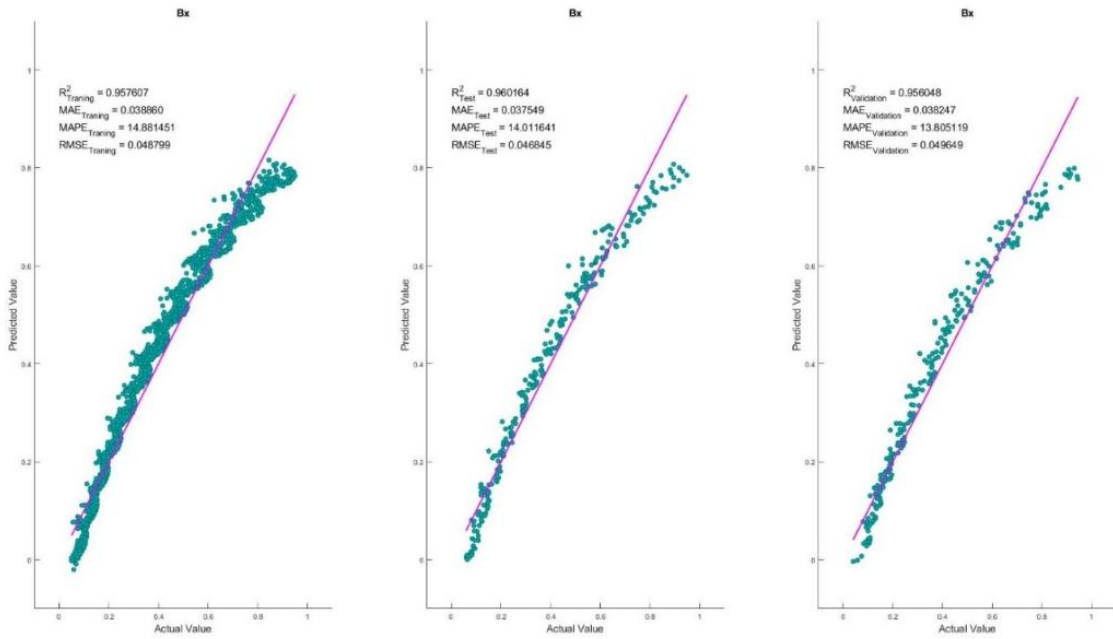
Figure 6-15: B_x ANN scatter plots a) Train b) Test c) Validation sets

As displayed in Figure 6-16, seven neurons are required to approximate the B_y function. Despite high R^2 values on all three sets, as Figure 6-17 shows, the residual increases by moving further from the center as expected.
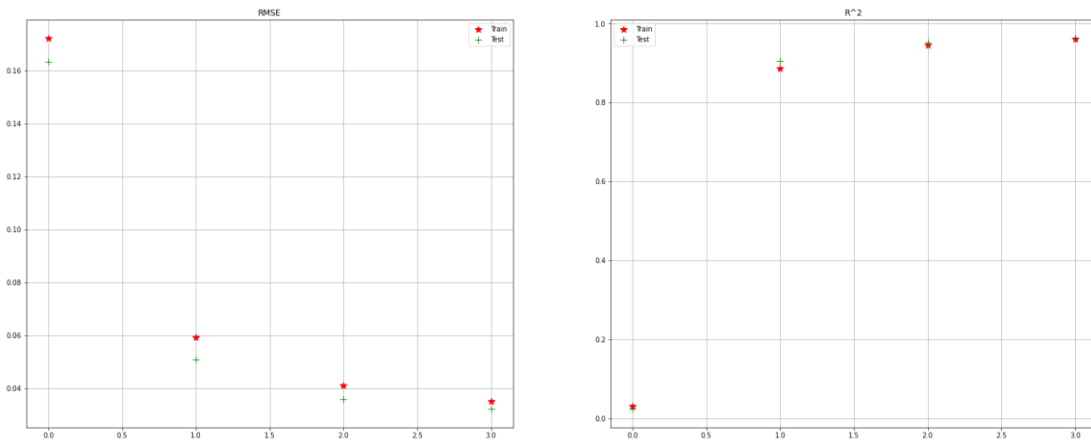
Figure 6-16: ANN for B_y a) $RSME$ b) R^2
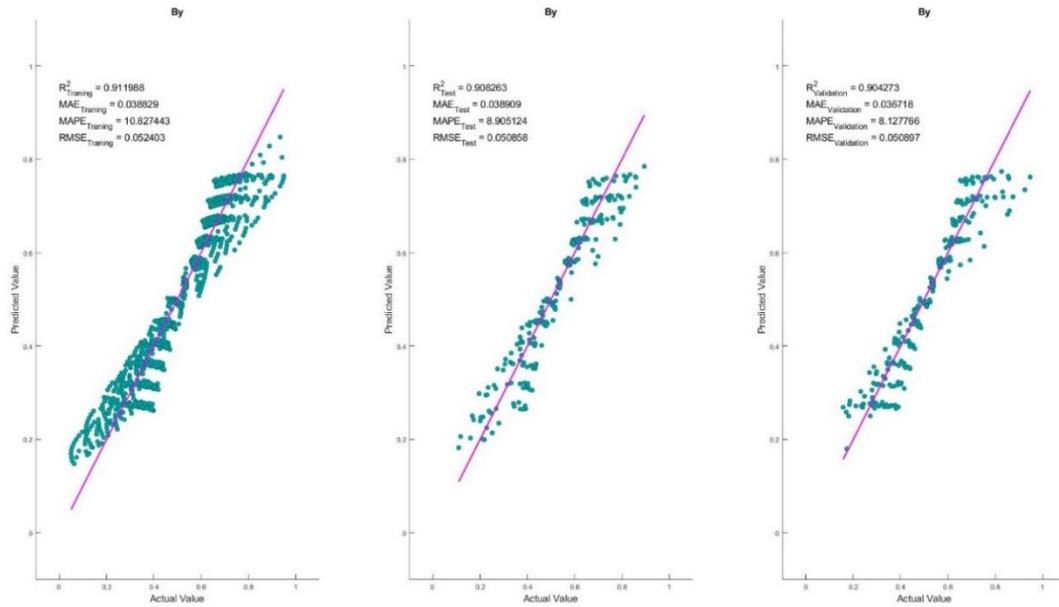
Figure 6-17: B_y ANN network scatter plots a) Train b) Test c) Validation sets

Lastly, B_z had been approximated using this algorithm. As illustrated in Figure 6-18, six neurons are required to optimize the network performance. According to Figure 6-19, the reseals are higher when the output is less than 0.4. This network also provides an R^2 of more than 0.9 but high $RSME$ with respect to the output range.
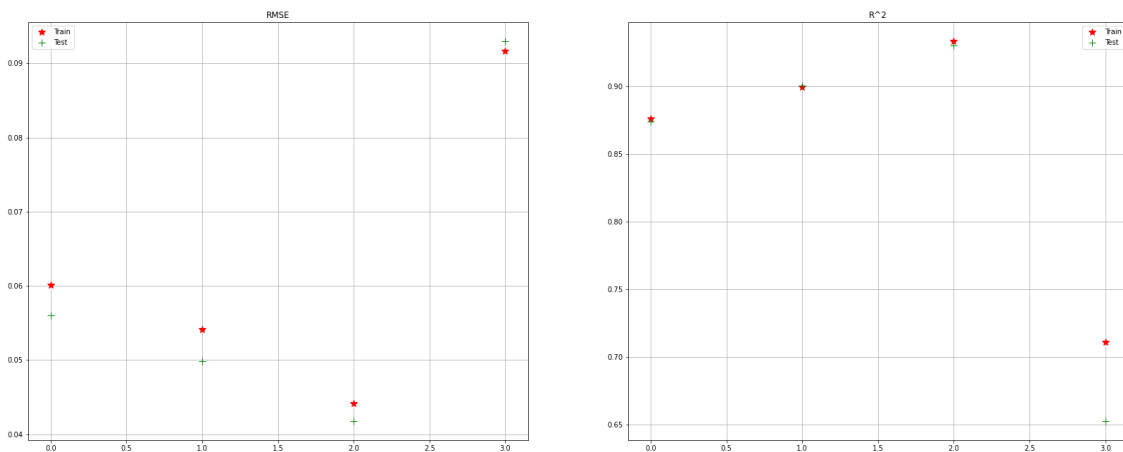
Figure 6-18: ANN for B_z a) $RSME$ b) R^2
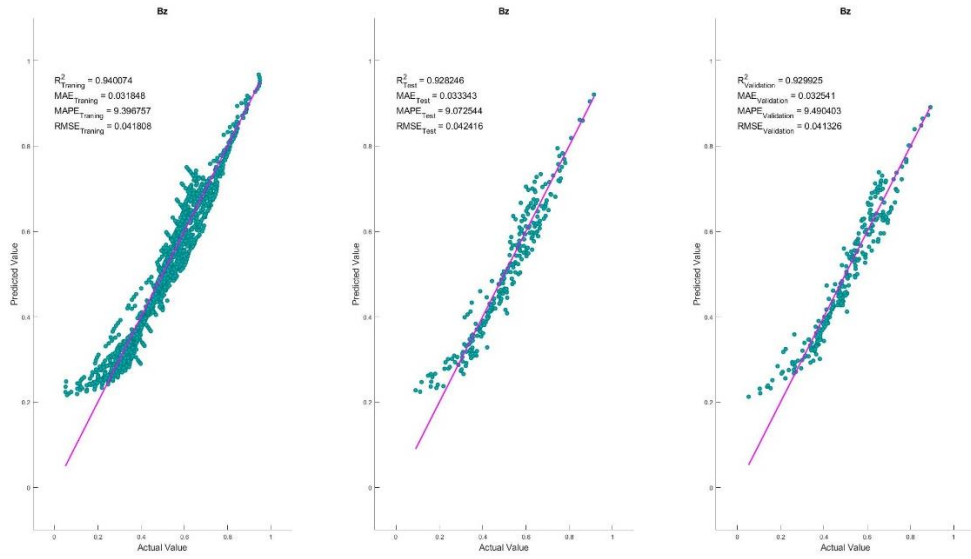
Figure 6-19: B_z ANN network scatter plots a) Train b) Test c) Validation sets

The optimum networks for each component had been summarized in Figure 6-20.
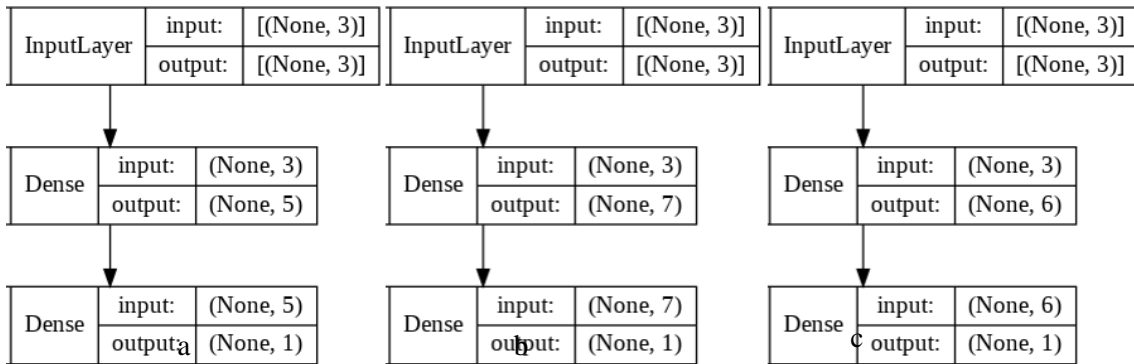
Figure 6-20: Optimized networks for a) B_x b) B_y c) B_z

6.5.3.2 Artificial Neural Network with Simulated Annealing (ANN/SA)

For the sake of similarity, the number of hidden layers remained one, and the number of neurons varied from four to seven. The optimizer used in this section is Levenberg Marquardt since it worked

better than gradient descent. The temperature cycles and acceptance constant have been fixed to fifteen and one thousand five hundred, respectively. Moreover, the initial temperature is 15, and the cooling temperature is equal to 0.015 for the temperature cycling cooling process.
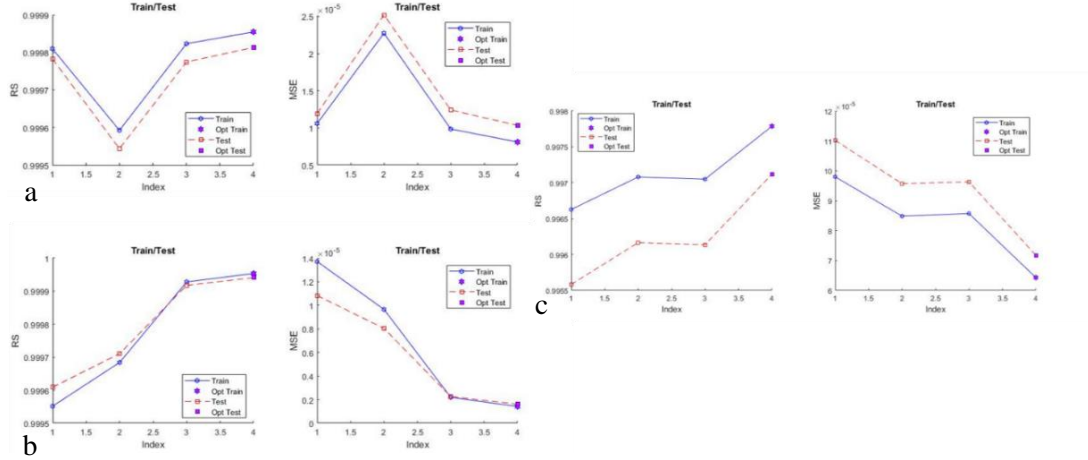
Figure 6-21: R^2 and $RSME$ for a)B_x b)B_y c)B_z of ANN/SA

According to Figure 6-21, all three components perform their best with seven neurons with an R^2 almost equal to one and the error order of 1e-5. If the validation set performs the same, they can be considered optimized networks. As Figure 6-22 indicates, the validation set performs similarly to the train and test sets; hence, seven neurons will be considered the optimum network for all three components. It worth mentioning that B_z with the normalized value in the range of 0.45 to 0.50 will have more errors than the rest.
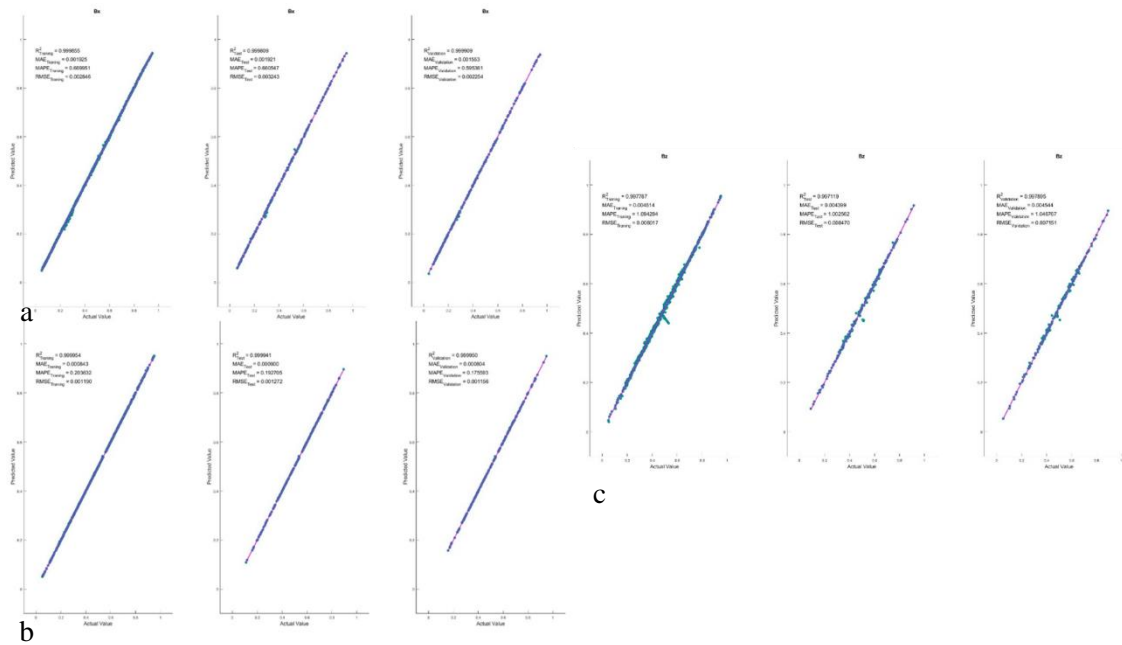
Figure 6-22: Scatter plots of a)B_x b) B_y c) B_z caused from ANN/SA results

6.5.3.3 Gene Expression Programming (GEP)

To develop the GEP algorithm, four different scenarios were considered. The constant two hundred chromosomes followed by seven or eight heads and three or four genes. Each node could have taken addition, subtraction, multiplication, division, square root, exponential, natural logarithm, inverse, square, min, max, average, arctangent, or tangent functions to form the GEP models.

According to Figure 6-23 a B_x reaches the best performance at the fourth scenario where head size and the number of genes are equal to eight and four, respectively; however, three genes perform better on the test dataset. Since the main reason for using the test set is to evaluate the performance of the hyperparameters, and three genes are the second-best performance on the training set, three genes are considered as the optimum hyperparameter for B_x.

Both train and test sets optimally perform on similar scenarios for the other two components. By reaches its best performance with eight as head size and three genes while B_z's optimal performance is associated with seven heads and four genes.
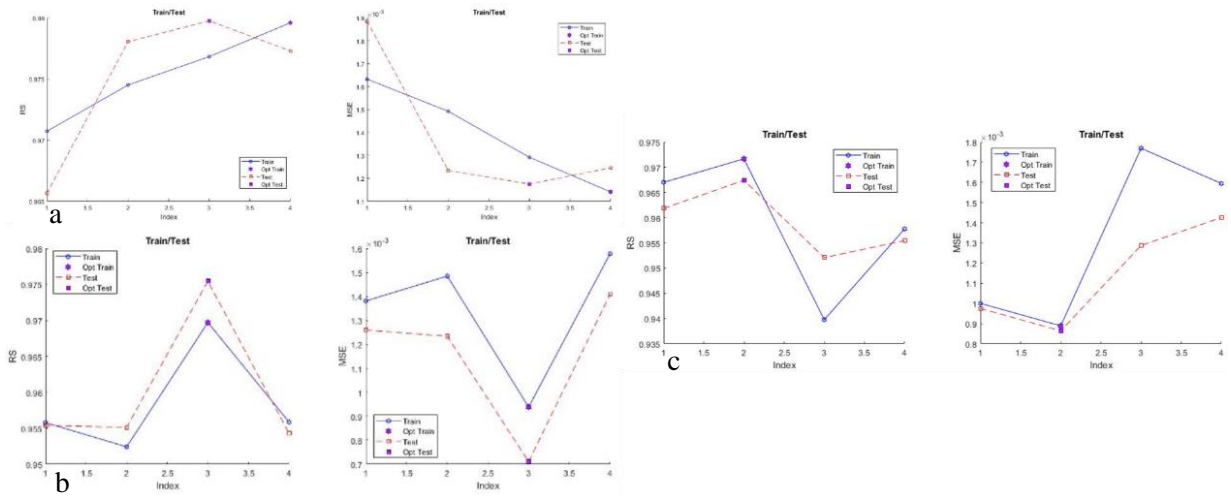
Figure 6-23: R^2 and $RSME$ for a)B_x b) B_y c) B_z of GEP

According to Figure 6-24, the GEP is also an acceptable approximation for the field values; however, the $RMSE$ values seem high. For B_x with more than 0.7, B_y with less than 0.3 normalized values, the error increases considerably.
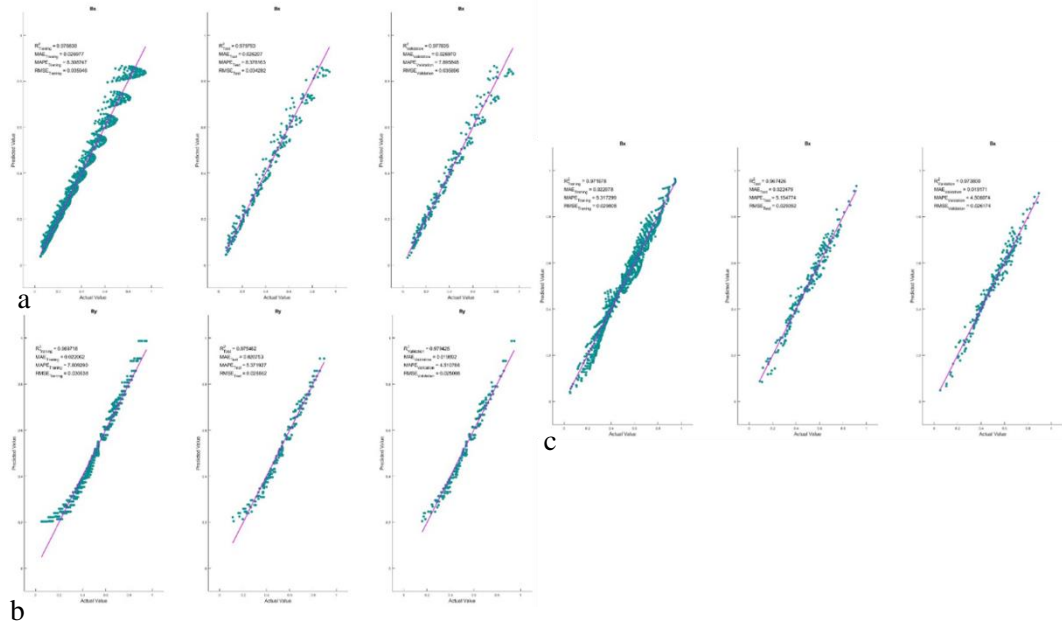
Figure 6-24: Scatter plots of a) B_x b) B_y c) B_z caused from GEP results

Figure 6-25 shows the expression trees of each solution. The connection link between genes is the addition operation; hence, the final equation will be the summation of genes. Equations (90), (91), and (92) are the analytical models created by GEP, and Table 6-4 includes the associated constants.
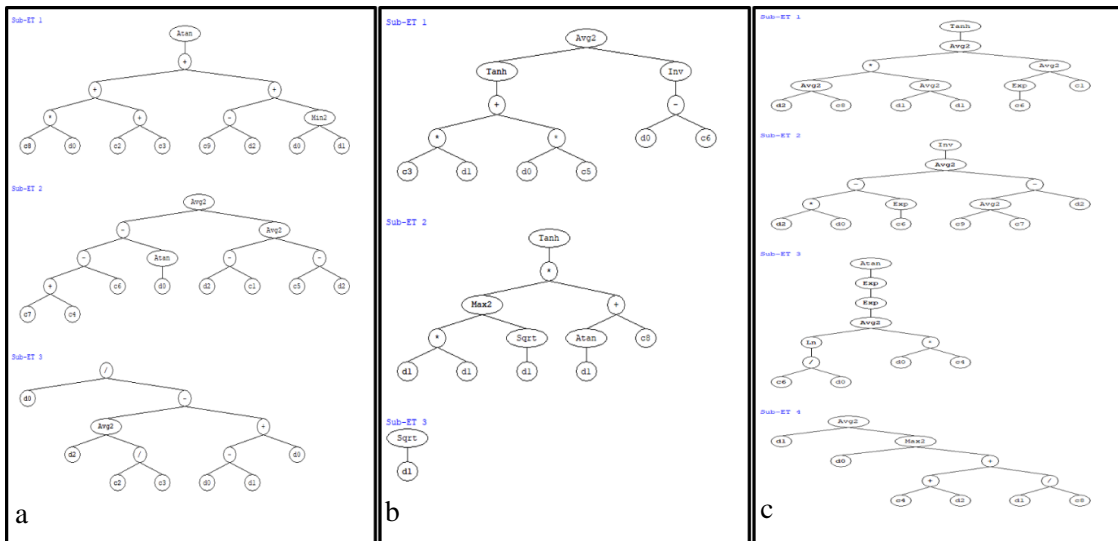
Figure 6-25: Expression trees for a) B_x b) B_y c) B_z

76

$$Bx = \text{atan}((((G1C8 \times Px) + (G1C2 + G1C3)) + ((G1C9 - Pz) + \min(Px, Py))))$$
$$+ (((((G2C7 + G2C4) - G2C6) - \text{atan}(Px)) + (((Pz - G2C1) + (G2C5$$
$$- Pz)) \tag{90}$$

$$By = ((\tanh(((G1C3 \times Py) + (Px \times G1C5))) + (1/((Px - G1C6))))/2) + \tanh((\max((Py$$
$$\times Py), realsqrt(Py)) \times (\text{atan}(Py) + G2C8))) + realsqrt(Py) \tag{91}$$

$$Bz = \tanh((((((Pz + G1C8)/2.0) \times ((Py + Py)/2)) + ((exp(G1C6) + G1C1)/2))/2))$$
$$+ (1/(((((Pz \times Px) - exp(G2C6)) + (((G2C9 + G2C7)/2) - Pz))/2)))$$
$$+ \text{atan}(exp(exp(((reallog((G3C6/Px)) + (Px \times G3C4))/2))))) + ((Py \tag{92}$$
$$+ \max(Px, ((G4C4 + Pz) + (Py/G4C8))))/2);$$

Table 6-4: Constant values of models generated by GEP

B_x	B_y	B_z
G1C8 = -9.70019259621326	G1C6 = -2.85744804223762	G1C1 = 0.443910086540932
G1C2 = -5.19798490013683	G1C3 = 2.64684130375072	G1C8 = -2.68844722194645
G1C3 = 1.59320418097797	G1C5 = 1.78276762172495	G1C6 = -6.12365323447602
G1C9 = 0.310305964130721	G2C8 = -2.12751407359647	G2C6 = -6.724470535726063
G2C6 = 1.02511365795162		G2C9 = 1.04723317147104
G2C1 = 0.241281795227256		G2C7 = -3.51484218655232
G2C5 = 1.80341098515976		G3C4 = 1.09169983645286
G2C7 = -3.27476309195044e-02		G3C6 = 2.58125294255938
G2C4 = 4.72411420026246		G4C4 = -0.508522610253914
G3C2 = -5.31158004067212		G4C8 = -4.08357290935277
G3C3 = 1.0678006810901		

6.5.4 Final algorithm selection

After developing thirty-six scenarios and selecting the best nine, the best three algorithms among all categories should be selected for the magnetic field approximation. Table 6-5 summarizes all the selected algorithms for each component, where green, yellow, and red indicate the best, a mediocre, and the worst performance. As shown, the ANN/SA has considerably better results than the other two algorithms; hence, it will be utilized to predict the magnetic field.

Table 6-5: The performance measurements of the selected algorithms

		Train			Test			Validation		
		ANN	ANN/SA	GEP	ANN	ANN/SA	GEP	ANN	ANN/SA	GEP
B_x	RS	0.957607	0.999855	0.976838	0.960164	0.999809	0.979763	0.956048	0.999909	0.977635
	RMSE	0.048799	0.002846	0.035946	0.046845	0.003243	0.03482	0.046845	0.002254	0.035896
	MAE	0.03886	0.001925	0.026977	0.037549	0.001921	0.026207	0.037549	0.001553	0.02697
	MAPE	14.88145	0.669951	8.308747	14.01164	0.660547	8.376163	14.01164	0.595361	7.895848
B_y	RS	0.911988	0.999954	0.969718	0.908263	0.999941	0.975462	0.900443	0.99995	0.979425
	RMSE	0.052403	0.00119	0.030638	0.050858	0.001272	0.026662	0.050897	0.001156	0.025008
	MAE	0.038829	0.000843	0.022062	0.038909	0.0009	0.020753	0.036718	0.000804	0.019882
	MAPE	10.82744	0.203632	7.80929	8.905124	0.192705	5.371927	8.127766	0.175593	4.510766
B_z	RS	0.940074	0.997787	0.971678	0.928246	0.997119	0.967426	0.929925	0.997895	0.9738
	RMSE	0.041808	0.008017	0.029808	0.042416	0.00847	0.029392	0.041326	0.007151	0.026174
	MAE	0.031848	0.004514	0.022078	0.033343	0.004399	0.022479	0.032541	0.004544	0.019171
	MAPE	9.396757	1.094284	5.317299	9.072544	1.002562	5.154774	9.490403	1.046767	4.506074

However, before the implementation, the predictive ability of the selected algorithm can be checked to ensure that the results can be utilized. Table 6-6 indicates that the additional performance measurements of the ANN/SA algorithm are in the expected zone of each criterion.

Table 6-6: Additional Validation

	Bx	By	Bz	condition
k	1.0001	1.0001	1.0007	$0.85 < k$ < 1.15
k'	0.99987	0.99988	0.99909	$0.85 < k'$ < 1.15
Ro^2	1	1	1	$close\ to\ 1$
Ro'^2	1	1	1	$close\ to\ 1$
m	$-9.1008E-05$	$-5.0262E-05$	-0.0021087	$|m| < 0.1$
n	$-9.1003E-05$	$-5.0261E-05$	-0.0021084	$|n| < 0.1$

6.6 Actuation

Magnetic field value prediction in the ROI enables developing an actuation logic, for the system shown in Figure 6-26, that relates the state of an agent to the current passing through each coil. As indicated in Figure 6-27, the agent is a disk magnet with a diameter and thickness of 0.1 and 0.0625 inches, respectively—also, a dipole moment of 0.0084 (A m2). Moreover, the position is collected in real-time using a laser sensor connected to the controller directly, which allows a 1D manipulation.
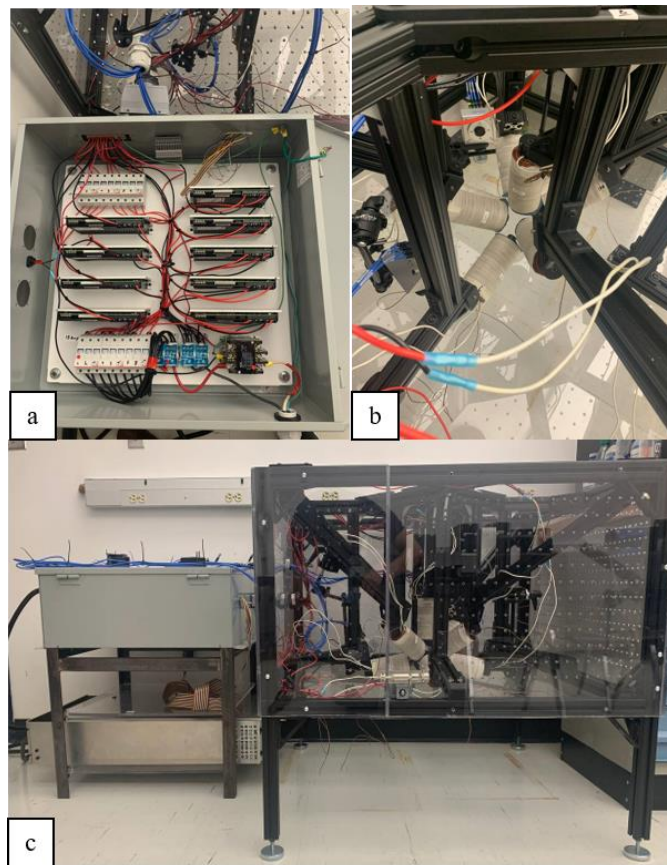

Figure 6-26: a) Electrical Equipment b) Coil configuration c) Completed system

The control process starts with getting the agent's position from the laser sensor and feeding it to the controller. The voltage of the laser sensor has a linear relationship with the distance of an object in front of it, where zero volts is associated with eighty millimeters, minus six volts indicate sixty-five millimeters, and four and seventy-two hundredth volts display a ninety-five millimeters distance from the agent to the laser. The distance element of the sensor in the voltage-distance relationship was mapped to the distance variable in the working space, where 80mm distance from the laser is associated with zero. The voltage-distance relationship in ROI is formulated in (93):

$$y = 2.7884 \times v - 0.09401$$

(93)

Where y is the P_y component of the agent's position vector in ROI, and v is the voltage produced by the sensor.
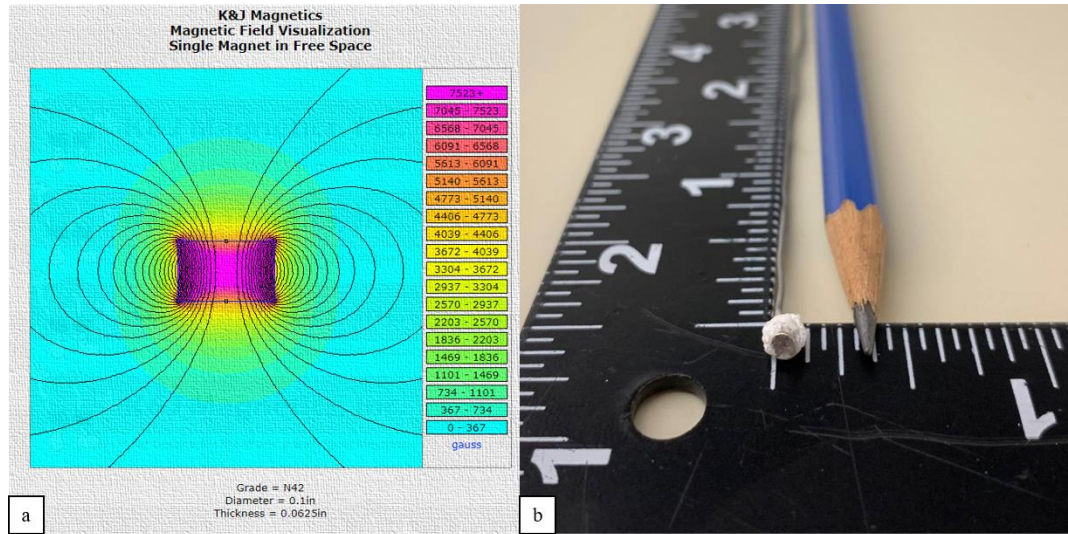

Figure 6-27: a) The agent's dimensions from manufacturer[63] b) the agent

The current state of the robot will be fed to the actuation matrix formulated in (27) to form the magnetic field and required gradient values.

$$\vec{W} = \begin{bmatrix} \vec{\tau} \\ \vec{F} \end{bmatrix}_{6\times1} = \begin{bmatrix} S(\vec{m})_{3\times3} & 0_{3\times5} \\ 0_{3\times3} & h(\vec{m})_{3\times5} \end{bmatrix}_{6\times8} \begin{bmatrix} \vec{B}(p) \\ G(p) \end{bmatrix}_{8\times N} I_{N\times1} \qquad (27)$$

If:

$$A(m,p) = \begin{bmatrix} S(\vec{m})_{3\times3} & 0_{3\times5} \\ 0_{3\times3} & h(\vec{m})_{3\times5} \end{bmatrix}_{6\times8} \begin{bmatrix} \vec{B}(p) \\ G(p) \end{bmatrix}_{8\times N} \qquad (94)$$

Hence:

$$I = A(m,p)^{\dagger}W \qquad (95)$$

Where $A(m,p)^{\dagger}$ is the pseudoinverse of the $A(m,p)$.

Then the difference between the desired and current state of the robot will be integrated with the PI controller to convert the position and the orientation difference to the wrench required in (95). Since the wrench value will directly affect the amount of total current and there are only 30 amps current valuable in total, the gain values for the PI controller should result in a total current less than 30ams. For half-millimeter movement in one direction, the gains are specified as:

$$k_p = 3.25$$

and

$$k_i = 0.01$$

As Figure 6-28 illustrates, this process continues till the robot reaches the desired state, and the wrench is almost equal to zero [14].
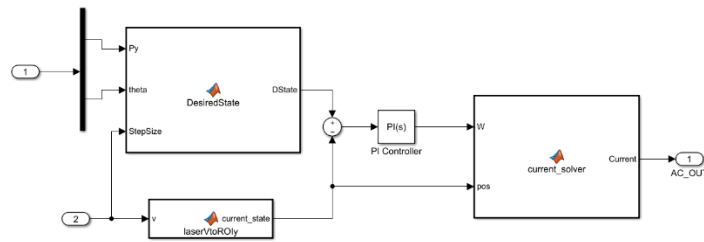

Figure 6-28: Actuation logic

In this logic, the output of the laser-which represents the current state of the agent-first, will be compared with the desired point, P_d. If the current location was less than P_d, 10% of the desired point will be added to the current position and will be considered the next step, and this process continues until the agent reaches or passes the desired point whit in less than 10% of the desired point. Therefore, the current and desired location difference is constant, meaning that PI gains will require almost constant wrench value from the actuation matrix. This logic can be used for manipulations that require constant force and torque values like penetrating a tissue on bone.

As Figure 6-29 indicates, the agent has started its movement from $\overrightarrow{P_0} = [0\ 0.0374\ 0]'$ and has reached the final destination of $\overrightarrow{P_f} = [0\ .513\ 0]'$. Although the laser still detects an error of 0.013 mm, the generated force of this difference cannot overcome the system's friction and agent's weight. Therefore, the agent stabilizes at its final destination with 13 μm accuracy.
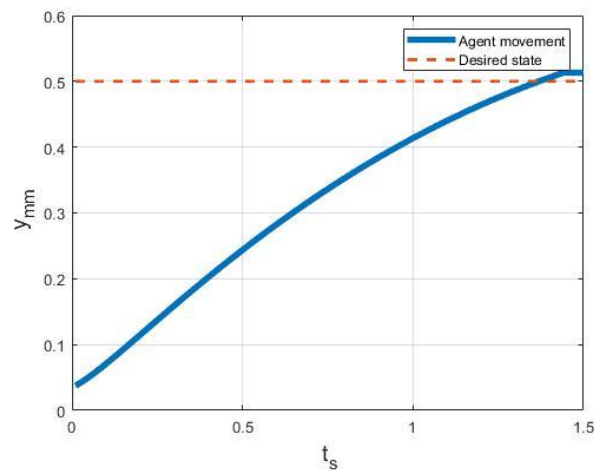
Figure 6-29: Agent Movement

This experiment approves the system's functionality with an error of 13 μm. A few factors are causing this error, including friction, hanging weight of the attached piece to the agent, and lack of information

from the other axis. The actuation logic has been implemented assuming that the system is located at the center of the working space; however, the only detected location is y-axis. Therefore, the actuation matrix is solved for the initial point of $[0 \ 0.0374 \ 0]'$, whereas it is worth mentioning that $[0 \ 0.0374 \ Pz]'$ is the actual location of the agent, where Pz had been eyeballed to zero. The performance can be enhanced by implementing the position and orientation of the agent using cameras where all the required information can be extracted.

Chapter 7

Conclusion

This chapter will provide a brief discussion over each phase of the project and summarize the accuracy of the system's models and performance. Then few suggestions for future research will be provided.

7.1 Discussion

The proposed system is designed with nine coils placed normal to a spherical workspace. This configuration resulted in developing a spatial constraint used in optimizing each coil's dimensions with respect to its power consumption and generated force over an agent with a volume of millimeter cube. G equal to 0.14 (with $\alpha = 3.3019$ and $\beta = 6.0761$) and force equal to 0.497 mN has resulted in a cylindrical iron-core with optimized dimensions.

The model developed for predicting a cylindrical axial coil's dimensions and total wire length has just less than 2.5 percent error and is sufficiently accurate. Utilizing the model for calculating resistance has generated less than 5 percent error. Moreover, the radius of 60 mm for working space allows coils to perform in their linear region; therefore, the superposition concept can be applied for measuring the total force and torque caused by each coil.

A frame that resists the vibration caused by the passing current through coils had been designed and manufactured to hold the coils. The vibration should have been absorbed since two cameras are attached to the frame, and any unwanted movement would have caused disfavored noise to their output. The manufactured frame also provides easy access to the coils and enables effortless coil movement along the coil's holder arm using a pin-hole system.

Furthermore, the entire system provides a safe operation environment as every piece of equipment consuming more than 100 Watts, or 40 volts are enclosed for safe operation. Moreover, an extra safety relay/ limit switch circuit is embedded to cut the circuit in undesirable operations. Also, to ensure that the back emf voltage does not damage the equipment, a diode has been used. To specify the properties of the diode, three different experiments have been developed to measure the coil's inductance.

Since torque and force values at each point are a function of the magnetic field and current also in this work, magnetic field and current are considered linearly related; only a model for magnetic field values have replaced FEM simulation results. Moreover, the FEM model of the coils has been altered by ANN/SA regression model. The dataset used for training and validating the algorithms has been collected utilizing a gauss meter attached to a micromanipulator over a coil energized by one amps current passing through it.

All three methods showed promising performances and could have been implemented; however, ANN/SA has shown magnificent performance - the R^2 of 0.99 and RMSE in order of 0.001. Six additional performance measurements had been evaluated to guarantee the predictability of the developed algorithm, and the results were completely sufficient.

The magnetic field created by each coil had been successfully approximated and utilized to perform a simple 1D manipulation task using a laser sensor. With $K_p = 3.25$ nad $k_i = 0.01$ system could move the agent in the desired direction with $13\mu m$ accuracy

86

7.2 Future work

This system can accommodate various coil shapes and dimensions placed at different distances; hence, it can be utilized for various research implementations.

- The effect of coils with different shapes and sizes on the controllability of the ROI can be investigated.

- By expanding the data collection region using a proper manipulator such as Panda, the movability of the agent can be expanded.

- A system of hall sensors can be developed and placed in the working space to measure the magnetic field of each coil individually. The measured magnetic fields for each coil are produced not only by the coil with running current through it but also by the magnetized cores of the other coils. The prediction model based on this approach enables researchers to capture the non-linearity that considered nominal meanwhile implement the superposition method to measure the required current for each coil individually.

- Cameras can be used to provide position and orientation feedback to enhance the controllability of the agent.

- Heat cameras can be used to navigate the agent inside a box with non-clear surfaces.

- Different agent configurations can be designed and fabricated to do simple surgical takes like cutting or drilling soft tissue.

References

[1]   M. Kamal, J. Shang, V. Cheng, S. Hatkevich, and G. S. Daehn, "Agile manufacturing of a micro-embossed case by a two-step electromagnetic forming process," *J. Mater. Process. Technol.*, vol. 190, no. 1–3, pp. 41–50, 2007, doi: 10.1016/j.jmatprotec.2007.03.114.

[2]   A. Sarkar, M. A. Somashekara, M. P. Paranthaman, M. Kramer, C. Haase, and I. C. Nlebedim, "Functionalizing magnet additive manufacturing with in-situ magnetic field source," *Addit. Manuf.*, vol. 34, no. May, p. 101289, 2020, doi: 10.1016/j.addma.2020.101289.

[3]   Y. Jia, P. Zhao, J. Xie, X. Zhang, H. Zhou, and J. Fu, "Single-electromagnet levitation for density measurement and defect detection," *Front. Mech. Eng.*, vol. 16, no. 1, pp. 186–195, 2021, doi: 10.1007/s11465-020-0608-0.

[4]   D. Zhou, J. Wang, Y. He, D. Chen, and K. Li, "Influence of metallic shields on pulsed eddy current sensor for ferromagnetic materials defect detection," *Sensors Actuators, A Phys.*, vol. 248, pp. 162–172, 2016, doi: 10.1016/j.sna.2016.07.029.

[5]   C. Qi, D. Han, and T. Shinshi, "A MEMS-based electromagnetic membrane actuator utilizing bonded magnets with large displacement," *Sensors Actuators, A Phys.*, vol. 330, p. 112834, 2021, doi: 10.1016/j.sna.2021.112834.

[6]   D. Liu *et al.*, "Magnetic driven two-finger micro-hand with soft magnetic end-effector for force-controlled stable manipulation in microscale," *Micromachines*, vol. 12, no. 4, 2021, doi: 10.3390/mi12040410.

[7]   E. Shameli, D. G. Craig, and M. B. Khamesee, "Design and implementation of a magnetically suspended microrobotic pick-and-place system," *J. Appl. Phys.*, vol. 99, no. 8, pp. 6–9, 2006, doi: 10.1063/1.2173950.

[8]   D. M. Stefanescu, *Handbook of Force Transducers Characteristics and Applications*.

Springer.

[9]   D.-K. Hong, Ki-Chang Lee, B.-C. Woo, and Dae-Hyun Koo, "Optimum design of electromagnet in magnetic levitation system for contactless delivery application using response surface methodology," pp. 1–6, 2009, doi: 10.1109/icelmach.2008.4800199.

[10]   S. Jeon *et al.*, "A Magnetically Controlled Soft Microrobot Steering a Guidewire in a Three-Dimensional Phantom Vascular Network," *Soft Robot.*, vol. 6, no. 1, pp. 54–68, 2019, doi: 10.1089/soro.2018.0019.

[11]   B. J. Nelson, I. K. Kaliakatsos, and J. J. Abbott, "Microrobots for minimally invasive medicine," *Annu. Rev. Biomed. Eng.*, vol. 12, pp. 55–85, 2010, doi: 10.1146/annurev-bioeng-010510-103409.

[12]   J. Giltinan and M. Sitti, "Simultaneous six-degree-of-freedom control of a single-body magnetic microrobot," *IEEE Robot. Autom. Lett.*, vol. 4, no. 2, pp. 508–514, 2019, doi: 10.1109/LRA.2019.2891080.

[13]   M. Sitti *et al.*, "Biomedical Applications of Untethered Mobile Milli/Microrobots," *Proc. IEEE*, vol. 103, no. 2, pp. 205–224, 2015, doi: 10.1109/JPROC.2014.2385105.

[14]   J. D. Keuning, J. De Vries, L. Abelmann, and S. Misra, "Image-based magnetic control of paramagnetic microparticles in water," *IEEE Int. Conf. Intell. Robot. Syst.*, pp. 421–426, 2011, doi: 10.1109/IROS.2011.6048703.

[15]   L. Wang, M. Dkhil, A. Bolopion, and P. Rougeot, "Applications," no. August, pp. 26–30, 2013.

[16]   S. Floyd, E. Diller, C. Pawashe, and M. Sitti, "Control methodologies for a heterogeneous group of untethered magnetic micro-robots," *Int. J. Rob. Res.*, vol. 30, no. 13, pp. 1553–1565, 2011, doi: 10.1177/0278364911399525.

[17]   B. Ioan, A. Ivan, G. Hwang, J. Agnus, and N. Chaillet, "NIST and IEEE Challenge for

MagPieR," *Robot. Autom. Mag. IEEE*, vol. 19, no. june, pp. 63–70, 2012.

[18]   M. P. Kummer, J. J. Abbott, B. E. Kratochvil, R. Borer, A. Sengul, and B. J. Nelson, "Octomag: An electromagnetic system for 5-DOF wireless micromanipulation," *IEEE Trans. Robot.*, vol. 26, no. 6, pp. 1006–1017, 2010, doi: 10.1109/TRO.2010.2073030.

[19]   G. A. Cole, K. Harrington, H. Su, A. Camilo, J. G. Pilitsis, and G. S. Fischer, *Closed-loop actuated surgical system utilizing real-time In-Situ MRI guidance*, vol. 79. 2014.

[20]   S. Yuan, Y. Wan, Y. Mao, S. Song, and M. Q. H. Meng, "Design of a novel electromagnetic actuation system for actuating magnetic capsule robot," *IEEE Int. Conf. Robot. Biomimetics, ROBIO 2019*, no. December, pp. 1513–1519, 2019, doi: 10.1109/ROBIO49542.2019.8961655.

[21]   A. J. Petruska and B. J. Nelson, "Minimum Bounds on the Number of Electromagnets Required for Remote Magnetic Manipulation," *IEEE Trans. Robot.*, vol. 31, no. 3, pp. 714–722, 2015, doi: 10.1109/TRO.2015.2424051.

[22]   V. N. T. Le, N. H. Nguyen, K. Alameh, R. Weerasooriya, and P. Pratten, "Accurate modeling and positioning of a magnetically controlled catheter tip," *Med. Phys.*, vol. 43, no. 2, pp. 650–663, 2016, doi: 10.1118/1.4939228.

[23]   E. Diller, J. Giltinan, and M. Sitti, "Independent control of multiple magnetic microrobots in three dimensions," *International Journal of Robotics Research*, vol. 32, no. 5. pp. 614–631, 2013, doi: 10.1177/0278364913483183.

[24]   "2010_Cardiology-Review-Remote-Navigation_Nguyen.Pdf." .

[25]   R. Yu *et al.*, "Modeling Electromagnetic Navigation Systems for Medical Applications using Random Forests and Artificial Neural Networks," *Proc. - IEEE Int. Conf. Robot. Autom.*, pp. 9251–9256, 2020, doi: 10.1109/ICRA40945.2020.9197212.

[26]   J. Edelmann, A. J. Petruska, and B. J. Nelson, "Estimation-Based Control of a Magnetic

Endoscope without Device Localization," *J. Med. Robot. Res.*, vol. 03, no. 01, p. 1850002, 2018, doi: 10.1142/s2424905x18500022.

[27] S. Hosseini, M. Mehrtash, and M. B. Khamesee, "Design, fabrication and control of a magnetic capsule-robot for the human esophagus," *Microsyst. Technol.*, vol. 17, no. 5–7, pp. 1145–1152, 2011, doi: 10.1007/s00542-011-1231-0.

[28] J. Franklin, *Classical Electromagnetism*. Pearson Addison-Wesley, 2005.

[29] X. Zhang, "Cooperative Manipulation Using a Magnetically Navigated Microrobot and a Micromanipulator," 2017.

[30] F. T. Ulaby, *Fundamentals of Applied Electromagnetics*. Pearson/Prentice Hall, 2007.

[31] S. Schuerle, S. Erni, M. Flink, B. E. Kratochvil, and B. J. Nelson, "Three-dimensional magnetic manipulation of micro-and nanostructures for applications in life sciences," *IEEE Trans. Magn.*, vol. 49, no. 1, pp. 321–330, 2013, doi: 10.1109/TMAG.2012.2224693.

[32] H. Tiegna, A. Bellara, Y. Amara, and G. Barakat, "Analytical modeling of the open-circuit magnetic field in axial flux permanent-magnet machines with semi-closed slots," *IEEE Trans. Magn.*, vol. 48, no. 3, pp. 1212–1226, 2012, doi: 10.1109/TMAG.2011.2171979.

[33] Y. Amara and G. Barakat, "Analytical modeling of magnetic field in surface mounted permanent-magnet tubular linear machines," *IEEE Trans. Magn.*, vol. 46, no. 11, pp. 3870–3884, 2010, doi: 10.1109/TMAG.2010.2053850.

[34] A. J. Petruska, A. W. Mahoney, and J. J. Abbott, "Short Papers," vol. 30, no. 5, pp. 1222–1227, 2014.

[35] I. S. Grant and W. R. Phillips, *Electromagnetism*. Wiley, 2013.

[36] B. W. Khalil, *Dynamics of Parallel Robots*, vol. 35, no. 0. 2015.

[37] M. Ceccarelli, *Multibody Mechatronic Systems*, vol. 54. 2018.

[38] Q. Yu, H. Tang, K. C. Tan, and H. Yu, "A brain-inspired spiking neural network model with

temporal encoding and learning," *Neurocomputing*, vol. 138, pp. 3–13, 2014, doi: 10.1016/j.neucom.2013.06.052.

[39]   J. Zupan, "Introduction to artificial neural network (ANN) methods: what they are and how to use them," *Acta Chim. Slov.*, vol. 41, pp. 327–327, 1994.

[40]   A. D. Dongare, R. R. Kharde, and A. D. Kachare, "Introduction to Artificial Neural Network (ANN) Methods," *Int. J. Eng. Innov. Technol.*, vol. 2, no. 1, pp. 189–194, 2012, [Online]. Available:

https://citeseerx.ist.psu.edu/viewdoc/download?doi=10.1.1.1082.1323&rep=rep1&type=pdf.

[41]   S. Agatonovic-Kustrin and R. Beresford, "Basic concepts of artificial neural network (ANN) modeling and its application in pharmaceutical research," *J. Pharm. Biomed. Anal.*, vol. 22, no. 5, pp. 717–727, 2000, doi: 10.1016/S0731-7085(99)00272-1.

[42]   N. Ivanova, V. Gugleva, M. Dobreva, I. Pehlivanov, S. Stefanov, and V. Andonova, "We are IntechOpen , the world ' s leading publisher of Open Access books Built by scientists , for scientists TOP 1 %," *Intech*, vol. i, no. tourism, p. 13, 2016.

[43]   H. Sahli, *An Introduction to Machine Learning*. 2020.

[44]   D. Abramson, M. Krishnamoorthy, and H. Dang, "Simulated annealing cooling schedules for the school timetabling problem," *Asia-Pacific J. Oper. Res.*, vol. 16, no. 1, pp. 1–22, 1999.

[45]   A. H. Alavi, M. Ameri, A. H. Gandomi, and M. R. Mirzahosseini, "Formulation of flow number of asphalt mixes using a hybrid computational method," *Constr. Build. Mater.*, vol. 25, no. 3, pp. 1338–1355, 2011, doi: 10.1016/j.conbuildmat.2010.09.010.

[46]   A. H. Gandomi, A. H. Alavi, D. M. Shadmehri, and M. G. Sahab, "An empirical model for shear capacity of RC deep beams using genetic-simulated annealing," *Arch. Civ. Mech. Eng.*, vol. 13, no. 3, pp. 354–369, 2013, doi: 10.1016/j.acme.2013.02.007.

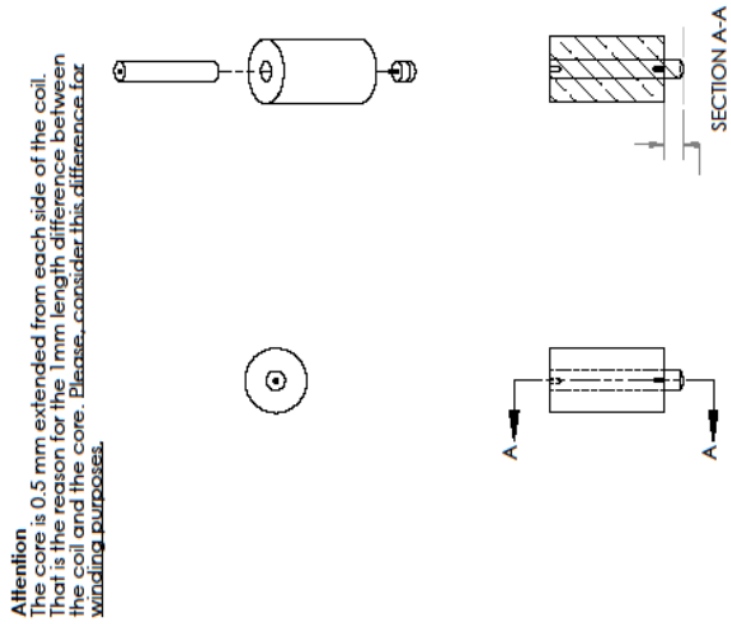[47]   A. H. Alavi and A. H. Gandomi, "Prediction of principal ground-motion parameters using a

hybrid method coupling artificial neural networks and simulated annealing," *Comput. Struct.*, vol. 89, no. 23–24, pp. 2176–2194, 2011, doi: 10.1016/j.compstruc.2011.08.019.

[48] C. Bento, A. Cardoso, and G. Dias, *Lecture Notes in Artificial Intelligence: Introduction*, vol. 3808 LNCS. 2005.

[49] C. Ferreira, *Gene Expression Programming*, 2nd ed. Springer.

[50] A. H. Gandomi, A. H. Alavi, M. R. Mirzahosseini, and F. M. Nejad, "Nonlinear Genetic-Based Models for Prediction of Flow Number of Asphalt Mixtures," *J. Mater. Civ. Eng.*, vol. 23, no. 3, pp. 248–263, 2011, doi: 10.1061/(asce)mt.1943-5533.0000154.

[51] Y. Murad *et al.*, "Flexural strength prediction for concrete beams reinforced with FRP bars using gene expression programming," *Structures*, vol. 33, no. April, pp. 3163–3172, 2021, doi: 10.1016/j.istruc.2021.06.045.

[52] L. Teodorescu and D. Sherwood, "High Energy Physics event selection with Gene Expression Programming," *Comput. Phys. Commun.*, vol. 178, no. 6, pp. 409–419, 2008, doi: 10.1016/j.cpc.2007.10.003.

[53] P. Gep, A. Neural, N. Ann, and F. Aslam, "Compressive Strength Prediction via Gene Expression," pp. 1–18, 2021.

[54] H. Majidifard, B. Jahangiri, P. Rath, L. Urra Contreras, W. G. Buttlar, and A. H. Alavi, "Developing a prediction model for rutting depth of asphalt mixtures using gene expression programming," *Construction and Building Materials*, vol. 267. 2021, doi: 10.1016/j.conbuildmat.2020.120543.

[55] N. J. Gogtay and U. M. Thatte, "Principles of correlation analysis," *J. Assoc. Physicians India*, vol. 65, no. MARCH, pp. 78–81, 2017.

[56] X. Wan, "Influence of feature scaling on convergence of gradient iterative algorithm," *J. Phys. Conf. Ser.*, vol. 1213, no. 3, 2019, doi: 10.1088/1742-6596/1213/3/032021.
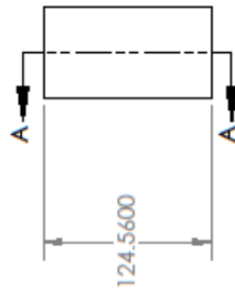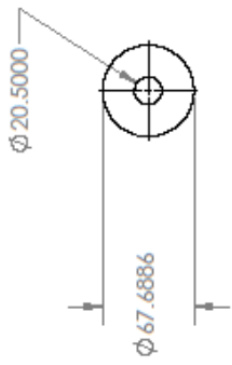
[57] "lggVP @ i.stack.imgur.com." [Online]. Available: https://i.stack.imgur.com/lggVP.png.

[58] A. Golbraikh and A. Tropsha, "<2000_Golbraikh_PredQSARdiversitySamplingTrainingTestSetSelection.pdf>," *Mol. Divers.*, vol. 2000, pp. 231–243, 2002.

[59] A. Golbraikh and A. Tropsha, "Beware of q2!," *J. Mol. Graph. Model.*, vol. 20, no. 4, pp. 269–276, 2002, doi: 10.1016/S1093-3263(01)00123-1.

[60] E. Shameli, "Design , Implementation and Control of a Magnetic Levitation Device," *Univ. Waterloo*, p. 199, 2008.

[61] J. N. Snyder and F. C. Grover, *Inductance Calculations Working Formulas and Tables*, vol. 18, no. 85. 1964.

[62] A. Pourkand and J. J. Abbott, "A Critical Analysis of Eight-Electromagnet Manipulation Systems: The Role of Electromagnet Configuration on Strength, Isotropy, and Access," *IEEE Robot. Autom. Lett.*, vol. 3, no. 4, pp. 2957–2962, 2018, doi: 10.1109/LRA.2018.2846800.

[63] "magfield @ www.kjmagnetics.com." [Online]. Available: https://www.kjmagnetics.com/magfield.asp?D=0.1&T=0.0625&L=&W=&OD=&ID=&calcType=disc&GRADE=42&surf_field=5154&rsurfC=&rsurfR=.

Appendix A

Coil blue prints

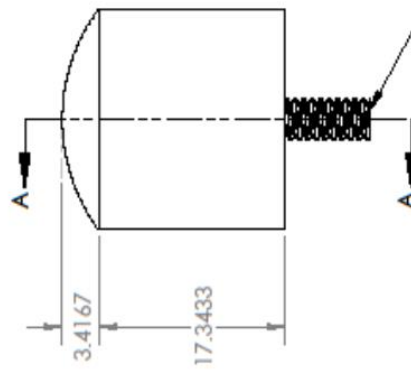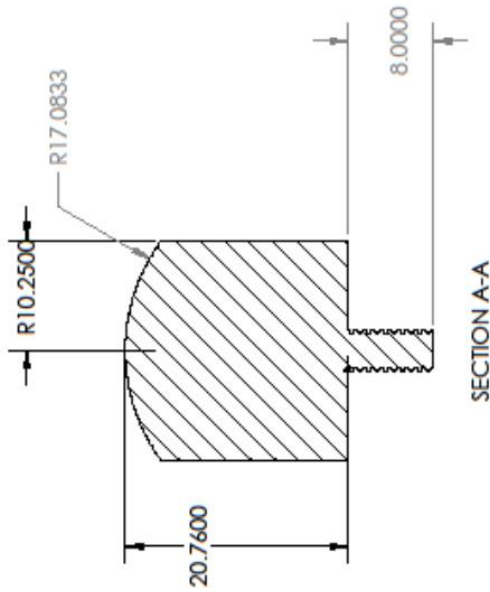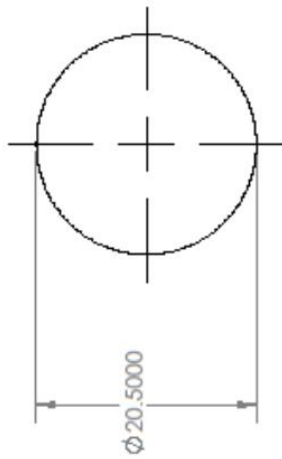| ITEM NO.	PART NUMBER	DESCRIPTION	QTY.
1	Coil	AWG 14 Number of Layers 14 Number of turns 72 N=1008 Hight=124.56mm Dout=67.6886mm Din=20.5mm Required = Thermostatic Sensor	10
2	Core	Hight=125.56mm Din=20.5mm	10
3	Core_Extention		10

Attention:
The core is 0.5 mm extended from each side of the coil. That is the reason for the 1mm length difference between the coil and the core. Please, consider this difference for winding purposes.

SECTION A-A

ITEM NO.	PART NUMBER	DESCRIPTION	QTY.
1	OneCoil	AWG 14 Number of Layers 14 Number of turns 72 N=1008 Hight=124.56mm Dout=67.6886mm Din=20.5mm Required = Thermostatic Sensor	10

SECTION A-A
SCALE 1 : 4

ϕ 20.5000

ϕ 67.6886

124.5600

A

A

ITEM NO.	PART NUMBER	DESCRIPTION	QTY.
1	Core_Extention	Threated part needs to fit with 10-32 hole on the core Material= Pure Iron	10

R17.0833

R10.2500

8.0000

20.7600

SECTION A-A

Ø20.5000

3.4167

17.3433

A

A
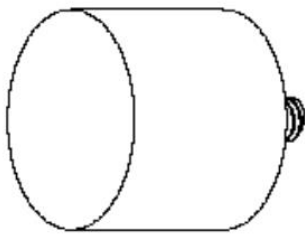
Should fit the 10-32 hole on the core

97

ø 5.1054 ∇ 12.7500
1/4-20 UNC ∇ 12.7000

ø 4.0386 ∇ 8.2000
10-32 UNF ∇ 8.0000

12.7700

8.0000

SECTION A-A
SCALE 1 : 4

125.5600

10.2500

A

A

125.5600

ø 20.5000
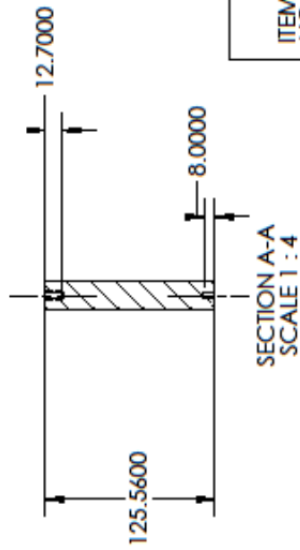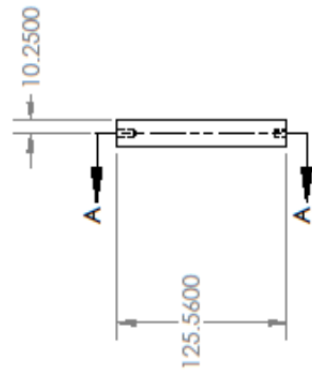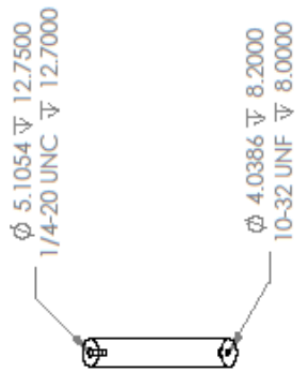
ITEM NO.	PART NUMBER	DESCRIPTION	QTY.
1	Core	Pure Iron	10

98